Electromagnetic properties of ferrites

ELECTROMAGNETIC PROPERTIES OF FERRITES

R. METSELAAR
Philips Research Laboratories,
Eindhoven,
The Netherlands

Abstract

ELECTROMAGNETIC PROPERTIES OF FERRITES.

Electromagnetic properties of ferrites are discussed, with special regard to the garnet and spinel structures. In the compound yttrium iron garnet, $Y_3Fe_5O_{12}$, small amounts of tetravalent dopants, like silicon, induce charge compensating Fe^{2+} ions. A discussion is given of the time-dependent magneto-crystalline anisotropy caused by the presence of the Fe^{2+} ions. At temperatures below about 100K, a number of physical properties of silicon-doped iron garnets can be changed by irradiation with infrared light. Examples are given of photoinduced changes in magnetocrystalline anisotropy, magnetic susceptibility and coercive force. Further, we discuss related photoinduced changes in the optical absorption coefficient and in linear dichroism. The effects are divided into two different classes: I) photoinduced effects which depend on the direction of the magnetization with respect to the crystallographic axes and the polarization direction of the incident light, and II) photo-induced effects that occur regardless of the prevailing magnetization distribution. In case I the effects are due to an unequal distribution of Fe^{2+} ions over sites which have a different orientation of their local symmetry axis with respect to the magnetization direction. In case II the photoinduced effects are due to a redistribution of Fe^{2+} ions over sites at different distances from the electron donating centre, e.g. the Si^{4+} ion. Finally magneto-optic effects in ferrites are considered. After a discussion of the phenomenological theory, the Faraday effect in the microwave and infrared region and the Faraday and Kerr effects at optical frequencies are considered.

1. INTRODUCTION

In the preceding lectures electromagnetic properties of metals and semiconductors have been discussed. The subject under discussion this week is restricted to a more limited group of solids, called ferrites. As far as electrical conductivity is concerned these oxidic compounds are insulators or semiconductors, but the essential property is their ferrimagnetic behaviour. The emphasis in my talks is on the influence of electromagnetic waves on the magnetic properties.

The term ferrite is used to indicate all magnetic oxides, independent of their crystal structure but containing iron oxide as their main component. In the introduction we shall first look at the parameters that are relevant to the

ferrimagnetic interactions in these compounds, after which we shall discuss the crystal structures of two important groups of materials. In section2 the influence of silicon doping on the magnetic anisotropy of yttrium iron garnet will be discussed, and in section 3 the optical absorption of this compound is given. Section 4 deals with photoinduced effects in garnets and spinel ferrites, and finally in section 5 magneto-optic effects will be discussed.

1.1. Magnetic interactions

Consider a collection of atoms with an electronic structure such that the atoms have a permanent magnetic moment [1.1]. If the coupling between the moments of the different atoms is small or zero, we find a paramagnetic behaviour. If the coupling between the atomic moments is large, we can distinguish three different cases: ferromagnetism, antiferromagnetism and ferrimagnetism. If the moments are aligned parallel, the material is called ferromagnetic. As a result of the coupling a spontaneous magnetization exists, i.e. even in the absence of a magnetic field there is a magnetic moment. Above a critical temperature, the ferromagnetic Curie temperature, the spontaneous magnetization vanishes. The material then behaves paramagnetically. The temperature dependence of the magnetization can be described using the molecular field theory proposed by Weiss. In this phenomenological theory it is assumed that each atomic moment experiences an internal magnetic field H_e that is proportional to the magnetization $\vec{M}$ which is produced by the neighbouring moments: $H_e = \lambda M$. The nature of the molecular field was first explained by Heisenberg. It was shown that the field is a result of the quantum mechanical exchange interaction. For two atoms having spins $\vec{S}_i$ and $\vec{S}_j$ the exchange Hamiltonian can be written as

$$\mathcal{H} = -2J_{ij}\ \vec{S}_i \cdot \vec{S}_j \tag{1.1}$$

where J_{ij} is the exchange integral. If the exchange interaction is restricted to nearest neighbours and if the exchange integral is isotropic, equal to J_e, we get

$$\mathcal{H} = -2J_e \sum_{ij}{}' \vec{S}_i \cdot \vec{S}_j \tag{1.2}$$

If J_e is positive, the energy is least when $\vec{S}_i$ is parallel to $\vec{S}_j$, i.e. the system shows ferromagnetic interaction. The exchange constant J_e is directly proportional to the Weiss constant λ. It follows from the theory that the Curie temperature is a direct measure of the exchange constant.

If the exchange constant J_e is negative, the configuration with lowest energy is that in which $\vec{S}_i$ is antiparallel to $\vec{S}_j$. This is the case in antiferro-

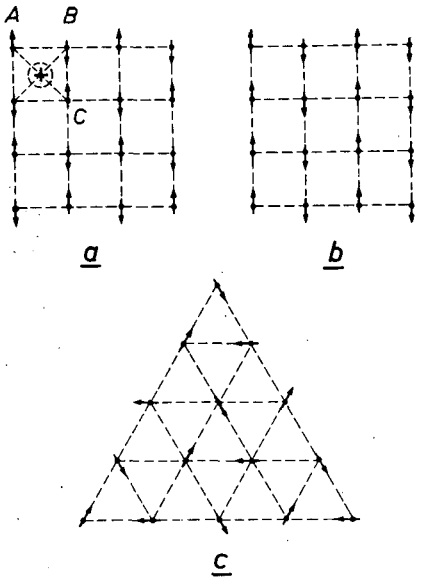

FIG.1.1. Two-dimensional representation of spin order for negative exchange energy J. In a) the A–B coupling is stronger than A–C; in b) it is weaker. In the trigonal lattice c) the spin order with three sublattices, the magnetizations of which make an angle of 120° with each other, has the lowest energy. (From: SMIT, J., WIJN, H.P.J., Ferrites, Philips Technical Library, Eindhoven, 1959.)

magnetic materials. A simple two-dimensional model is shown in Fig.1.1. The spin order depends not only upon the crystalline structure but also upon the ratios of the magnitudes of the interactions. In Fig.1.1a, for example, the interaction between the nearest neighbours A and B is stronger than between the next nearest neighbours A and C. In Fig.1.1b the reverse is true. In the trigonal lattice in Fig.1.1c the spin order can be described by three sublattices, the magnetizations of which make an angle of 120° with each other. In the cases a) and b) in Fig.1.1 the lattice can be divided into two sublattices. If the sublattices are occupied by identical ions, the net moment will be zero. This is the case in antiferromagnetic materials. If the magnetic moments of the sublattices differ in magnitude, or make an angle $\neq$ 180° with each other, a net moment will result. This case is known as ferrimagnetism. In the ferrites the ferrimagnetic type of ordering is usually found. We shall discuss oxides where the magnetic ions occupy two crystallographically different lattice sites. The discussion is limited to the case where the magnetization vectors on these two sites are aligned antiparallel, and accordingly the spontaneous magnetization is the difference of the magnetizations on the two

sublattices. Apart from this simple antiparallel spinconfiguration, many examples are known of materials with canted spinstructures or spiral spinstructures.

1.2. Magnetic anisotropies

1.2.1. Magnetocrystalline anisotropy

In the preceding section we have discussed only the mutual orientation of the magnetic moments, and have regarded the orientation in the crystal of the magnetization as arbitrary. In reality the magnetization vector in a ferro- or ferrimagnetic compound is bound to certain preferred crystallographic directions. This behaviour is described by the anisotropy energy, i.e. the energy needed to turn the magnetization vector $\vec{M}$ from a preferred direction (known as easy axis) into a difficult (or hard) direction. Let the direction be given by its direction cosines α_i with respect to the crystal axes. It has been found experimentally that the crystal anisotropy can be described by the first two or three terms of a power series in α_i. For a cubic crystal we have, for reasons of symmetry

$$E_K = K_1(\alpha_1^2\alpha_2^2 + \alpha_2^2\alpha_3^2 + \alpha_3^2\alpha_1^2) + K_2\,\alpha_1^2\alpha_2^2\alpha_3^2 + \ldots\ldots \tag{1.3}$$

The anisotropy constants K_1, K_2, etc. are material and temperature dependent. The constants can be determined by measuring the mechanical torque on a single crystal as a function of the direction of $\vec{M}$, or from ferromagnetic resonance data. The value and sign of the K's determine the direction where E_K is minimum. The cube diagonal [111], is such a preferred direction of magnetization if both $K_1 + (1/9)K_2 < 0$ and $K_1 + (4/9)K_2 < 0$ are satisfied. This is generally the case for the ferrites considered here.

For uniaxial crystals the expression for the anisotropy energy is

$$E_K = K_u \sin^2\theta + \ldots\ldots \tag{1.4}$$

where θ is the direction between the magnetization and the symmetry axis.

It follows from Eqs (1.3) and (1.4) that when the magnetization vector deviates from the preferred direction, the anisotropy energy increases. This can be described by saying that an effective field, the anisotropy field H_K, acts on the spins. For example, for $K_1 > 0$ the value of H_K is given by

$$H_K = 2K_1/M_s$$

The stiffness with which the magnetization is bound to the preferred directions also influences the field of the ferromagnetic resonance. The well-known resonance condition for the magnetization vector in a field H is $\omega_r = \gamma H$, where γ is the gyromagnetic ratio ($\gamma = g\mu_B/\hbar$), and ω_r the resonance frequency.

Due to the magnetic anisotropy the resonance field differs from this value. The resonance field is now given by

$$\omega_r = \gamma(H + H_K) \tag{1.5}$$

The measurement of the ω_r-H relation as a function of the direction of the applied field can be used to determine the anisotropy constants.

1.2.2. Origin of crystal anisotropy

The interaction energy between two magnetic dipoles is anisotropic. It is found, however, that the dipolar energy only takes account of a part of the experimentally observed K_1 values in uniaxial crystals. In cubic crystals with antiparallel spinstructure this interaction cannot contribute to the cubic constants K_1 or K_2. The occurrence of anisotropy in cubic materials and the additional terms in uniaxial materials must be explained in terms of spin-orbit interaction. It has been found that the anisotropy in the ferrites can be described in terms of the properties of the isolated magnetic ions. The influence of the surrounding ions on the electron orbitals of the magnetic ion is represented by the crystalline field. The surrounding magnetic ions interact via the exchange interaction, which is approximated by the field H_e.

Due to the crystalline field the electron orbits of the ion interact with the lattice. The spins of the electrons are coupled to the orbits by the spin-orbit interaction. Therefore, in order to understand the anisotropy, one has to consider the orbital states of the magnetic ions.

The orbital momentum of ions can be influenced strongly by the symmetry and the magnitude of the crystalline field. For instance Ni^{2+} ($3d^8$) and Cr^{3+} ($3d^3$), which have degenerate orbital ground states for the free ions, all have singlet ground states on octahedral sites in a crystal and therefore the orbital momentum is zero. As free ions Mn^{2+} and Fe^{3+} have already no orbital momentum anyway ($3d^5$ configurations). This means that for all these ions spin-orbit interaction in first order leads to a zero value of the anisotropy. Only higher order terms cause a small value of the anisotropy. On the other hand, Fe^{2+} ($3d^6$) and Co^{2+} ($3d^7$) on octahedral sites have a non-zero orbital momentum. The spin-orbit interaction now gives an appreciable magnetic anisotropy.

1.3. Magnetization processes

1.3.1. Magnetization curve

It is well known that in spite of the spontaneous magnetization of a ferro- or ferrimagnet the specimen may exhibit no magnetic moment when the applied field is zero. When a magnetic field is applied the magnetization may vary from zero to the saturation value. In order to explain this behaviour, Weiss introduced the concept of domains. Each domain is spontaneously magnetized, but the direction may vary from one domain to another. The net magnetization, which is the vector sum of the domain magnetizations, may take any value between zero and saturation.

If we measure the component of the magnetization along the direction of the applied field we generally obtain a curve like that shown in Fig.1.2. With the aid of this figure we shall describe a number of important material parameters.

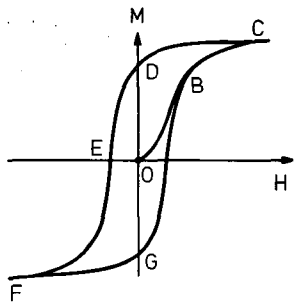

FIG.1.2. Magnetization curve (OBC) and hysteresis loop (CDEFGC) of a ferromagnetic or ferrimagnetic material.

We assume that the specimen is initially in the demagnetized state, indicated by the origin O of Fig.1.2. When a field is applied, the magnetization increases along the line OBC until the saturation value M_s is reached. The slope of this line in the origin $(dM/dH)_0 = \chi_i$, is called the initial susceptibility. When the field is decreased from the value indicated by the point C to zero, the magnetization decreases along CD. The point D is called the remanent magnetization value. An increase of the field in the reverse direction gives a zero magnetization in E. The field at this point is called coercive force H_c.

The complete curve CDEFGC, which is symmetric about the origin, is known as a hysteresis loop.

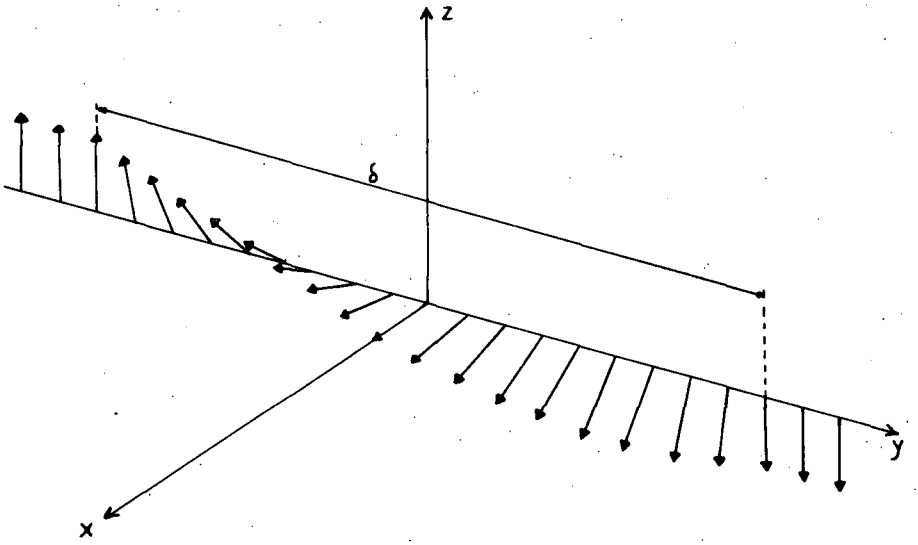

FIG.1.3. Spin structure of a 180° domain wall, wall thickness δ.

1.3.2. Domain structure

A uniformly magnetized sample shows free magnetic poles at its surface. On account of these free poles stray fields are present, which contribute to the magnetostatic energy E_d. By dividing the sample into domains this magnetostatic energy can be reduced considerably. In these domains the magnetization lies along a preferred direction. The uniformly magnetized domains are separated by a thin layer, the so-called domain wall or Bloch wall. In a domain wall the spins rotate from the preferential direction in the one domain into that of the second domain. The direction of the magnetization changes gradually as a result of the exchange interaction between neighbouring spins (Fig.1.3).

The wall energy E_w therefore consists of both exchange energy E_e and anisotropy energy E_K. A stable equilibrium is found if $E_w = E_K + E_e$ is a minimum. A calculation shows that the corresponding wall thickness, δ_w is given by

$$\delta_w \approx (2kT_c/aK)^{1/2} \tag{1.6}$$

Here k is the Boltzmann constant, T_c the Curie temperature (proportional to the exchange constant J_e), a the lattice constant, and K the anisotropy constant. The total wall energy per unit area of the wall is

$$E_w = 2K\delta_w \tag{1.7}$$

The geometry of the domain structure is determined by the requirement that the total energy must be minimum: $E_d + E_w = \text{minimum}$.

1.3.3. Domain boundary movement

The magnetization process described in Fig.1.2 can be discussed in terms of changes of domain configurations. In the demagnetized state O the domain magnetization vectors are distributed at random. The application of an external field contributes an energy term $E_h = \int \vec{M}.\vec{H}\, dv$. For small fields the minimization of the total energy is accomplished by small, reversible wall displacements. Let us assume that, due to imperfections in the crystal, the energy of a domain wall as a function of the position of the wall varies as shown in Fig.1.4. In the absence of the magnetic field, the wall stays at some minimum point where $\delta E_w/dx = 0$. The energy can be expressed to a first approximation as

$$E_w = \frac{1}{2} fx^2$$

in the vicinity of the minimum. The proportionality constant f is called the wall stiffness. Application of a small external field causes a displacement of the wall, with a corresponding change of the magnetization. The resulting initial susceptibility is given by

$$\chi_i = 4M_s^2 S/f \qquad (1.8)$$

where S is the total wall area per unit volume. This means that for small amplitudes of the applied field the susceptibility is inversely proportional to the wall stiffness f. From Fig.1.4 it is also obvious that if the magnetic field increases, the wall can for instance move suddenly to a position D. If the field is now allowed to decrease, the wall returns to a position C. This process of

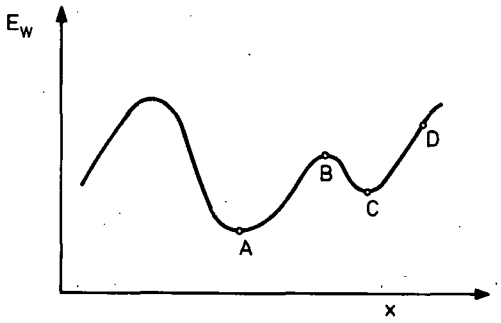

FIG.1.4. Wall energy E_w as a function of the position x of the wall.

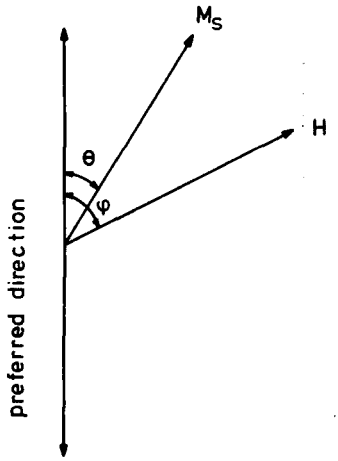

FIG.1.5. Rotation of the magnetization vector $\vec{M}_s$ due to an external field $\vec{H}$.

irreversible wall displacements leads to the hysteresis phenomena shown in Fig.1.2. The critical field strength is determined by the maximum value of the derivative of the wall energy:

$$H_c = \frac{1}{2M_s}\left(\frac{dE_w}{dx}\right)_{max}$$

This field will depend on the mechanism that determines the wall position. For actual samples a statistical treatment is necessary.

If there are no walls present, or if the walls are unable to move, magnetizing will take place as a result of the uniform rotation of all spins in the domain. Figure 1.5 illustrates the case of rotation for a sample with a uniaxial anisotropy. The component of M along the applied field divided by the value of the field is called the rotational susceptibility χ_{rot}. When the angle between the applied field and the preferred axis is φ, we get

$$\chi_{rot} = M_s \sin^2\varphi / H_K$$

For $\varphi < 90°$ the magnetization rotation will be reversible, for $\varphi > 90°$ an irreversible rotation occurs.

In general, the susceptibility χ (or the related quantity permeability, $\mu = 1 + 4\pi\chi$) consists both of domain wall displacement contributions and of rotational contributions.

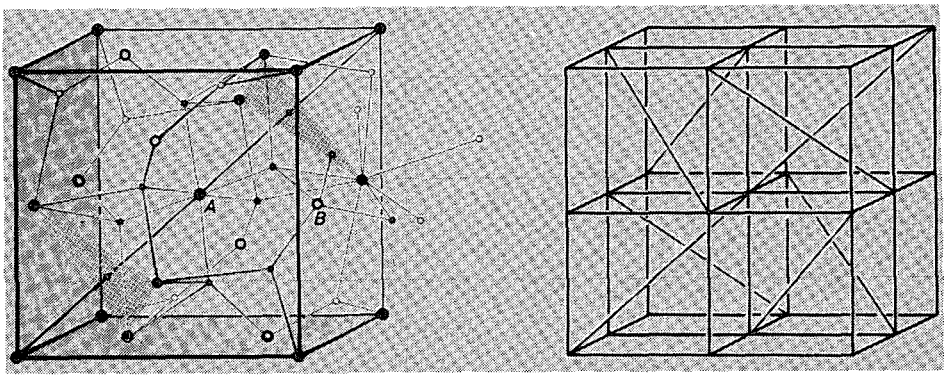

FIG. 1.6. Crystal structure of $Y_3Fe_5O_{12}$ (yttrium iron garnet). The right-hand picture gives the complete unit cell; the left-hand picture shows details of one octant. The indicated diagonals coincide with the local threefold axes. The full dots at the corners and in the centre of the cell are Fe^{3+} ions octahedrally coordinated by six oxygen ions (small dots and circles). The larger rings are tetrahedrally coordinated Fe^{3+} ions. The larger full dots are Y^{3+} ions. (From: Philips Tech. Rev. **31** *(1970) 33.)*

1.4. Crystal structures and magnetochemistry

The ferrites of greatest technical importance are derived crystallographically from three natural compounds: the spinel, the garnet and the magnetoplumbite. In this section the crystal structure of the garnet will be discussed in some detail, the spinel structure will be mentioned briefly.

1.4.1. Garnet structure

Garnet crystallizes in the cubic system and has a cubic body-centred lattice, space group $O_h^{10}\left(I\frac{4_1}{a}\bar{3}\frac{2}{d}\right)$.

The lattice constant of the iron garnets is about $a_0 \cong 12.5$ Å. There are three kinds of cation sites, all of which are occupied. As an important example we shall discuss the compound yttrium iron garnet (called YIG), $Y_3Fe_5O_{12}$. There are 8 formula units per unit cell, distributed as follows:

24 tetrahedral sites, (d-sites), occupied by Fe^{3+} ions,
16 octahedral sites, [a-sites], occupied by Fe^{3+} ions,
24 dodecahedral sites, {c-sites}, occupied by Y^{3+} ions.

Accordingly the ion distribution is

$$\{Y_3\}\ [Fe_2]\ (Fe_3)\ O_{12}$$

A three-dimensional representation of the structure is shown in Fig.1.6. In the immediate environment of an octahedral Fe^{3+} ion the Y^{3+} ions, which can be divided into two groups of three, define a local threefold axis. This local threefold axis coincides with one of the body diagonals of the lattice, the crystallographic ⟨111⟩ directions. Neighbouring Fe^{3+} ions in octahedral coordination always have a different one of the four possible ⟨111⟩ directions as local threefold axis.

In fact all three different polyhedra around the cations are distorted. The resulting site symmetry groups are C_{3i} for the octahedral cations, S_4 for the tetrahedral ions and D_2 for the dodecahedral ions.

In the ferrites, as in the majority of oxides, the distance between the metal ions is too great for a direct exchange to be possible. The theory of exchange in these compounds has been developed by Anderson [1.2]. The main feature of the Anderson theory is that the exchange between the cations takes place via the intermediate oxygen ion. The value of the exchange integral J depends on the overlap of the cation 3d wave functions with those of the anion 2p wave functions. This overlap is maximum for short Fe-O distances and Fe-O-Fe angles close to 180°. As a result the strongest interaction in YIG exists between Fe^{3+} on octahedral and Fe^{3+} on tetrahedral sites. This interaction is negative, i.e. the spins on the octahedral and tetrahedral sublattices are arranged anti-parallel. Per formula unit there are 3 Fe^{3+} on d-sites and 2 Fe^{3+} on a-sites, each contributing $5\mu_B$, so that the net moment is $5\mu_B$. The Curie temperature of YIG is 570 K. Since the Fe^{3+} ($3d^5$) has no orbital momentum, the crystalline anisotropy is zero in first order. In higher order the ground state recovers some orbital momentum by mixing with higher energy states via the spin-orbit interaction. This leads to a moderate value of the anisotropy. The preferred directions are the ⟨111⟩-axes of the crystal.

On all different sites of the garnet structure substitutions are possible. For instance yttrium can be replaced by most of the rare-earth ions, but also by Ca^{2+}, Pb^{2+}, Sr^{2+}. On the octahedral sites iron can be replaced by Al^{3+}, Ti^{4+}, Zr^{4+}, Hf^{4+}, Co^{2+} and Co^{3+}. Similarly for tetrahedral Fe^{3+} one can substitute Ga^{3+}, Si^{4+}, Ge^{4+}, V^{5+}. In general such substitutions do not take place on one site exclusively, but there is only a preferred occupation of the indicated positions.

Of special interest is the case of substitution of tetravalent ions. For instance, silicon can be substituted for iron to a maximum concentration of 0.5 Si^{4+} ion per formula unit. The electron donated by the silicon is found to be trapped on a ferric ion, i.e. for each Si^{4+} ion an Fe^{2+} ion is formed. The magnetic moment of Fe^{2+} ($3d^6$) is $4\mu_B$. Experimentally it is observed that the saturation magnetization at 0K of $Y_3\, Fe^{3+}_{5-2x}\, Fe^{2+}_x\, Si^{4+}_x\, O_{12}$ is given by $(5-4x)\,\mu_B$.

This can be explained if the Fe^{2+} ions are located in the octahedral sublattice.

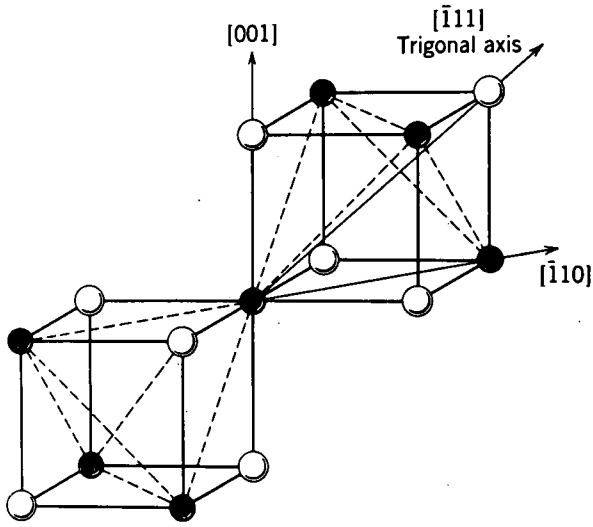

FIG. 1.7. Surrounding of the octahedral site of spinel structure. Open circles are oxygen ions, solid ones indicate cations.

In section 2 special attention will be paid to the influence of the ferrous ions on the magnetocrystalline anisotropy.

1.4.2. Spinel structure

The mineral spinel crystallizes in the cubic space group $O_h^7\left(F\frac{4_1}{d}\bar{3}\frac{2}{m}\right)$ with 8 molecules per unit cell. The spinel ferrites are derived from the mineral spinel $MgAl_2O_4$ by substituting Fe^{3+} for Al^{3+}. Any divalent cation with an ionic radius between about 0.6 and 1.0 Å can be substituted for Mg, according to the general formula $Me^{2+}\,Fe_2^{3+}\,O_4$. In the spinel lattice there are two kinds of lattice sites available for the cations: tetrahedral sites (A sites) and octahedral sites (B sites). The magnetic properties are governed by the strong negative exchange interaction between magnetic ions on A and B sites. The net moment of the ferrimagnetic compounds is therefore the difference between the moments on the A and B sublattices.

The surrounding of a tetrahedral ion by the other ions has strictly cubic symmetry (site group T_d). This is not the case for an individual octahedral ion. The octahedral ions, of course, are cubically surrounded as far as concerns the oxygen ions in the ideal lattice, but not as regards their environment by the neighbouring metal ions. Figure 1.7 shows the environment of a B ion by other B ions. The site group of an octahedral site is C_{3d}, the local [111] axis being the threefold symmetry direction. However, in the whole lattice cell all ⟨111⟩ directions occur equally, so that the overall symmetry remains cubic.

REFERENCES TO SECTION 1

[1.1] The topics of the introduction are discussed in textbooks such as: MORRISH, A.H., The Physical Principles of Magnetism, J. Wiley, New York (1965); CHIKAZUMI, S., Physics of Magnetism, J. Wiley, New York (1964); SMIT, J., WIJN, H.P.J., Ferrites, Philips Technical Library, Eindhoven (1959).

[1.2] ANDERSON, P.W., in Magnetism (RADO, G.T., SUHL, H., Eds), Vol.I, Academic Press, New York (1963).

2. MAGNETIC ANISOTROPY IN SILICON-DOPED YTTRIUM IRON GARNET

This section provides a necessary background to the light-induced effects which are discussed later. Emphasis is placed on the magnetic anisotropy of silicon-doped yttrium iron garnet, YIG:Si. A model is presented which describes the effects measured by magnetic resonance and torque magnetometer methods in terms of a thermally-activated valence exchange mechanism involving the ferrous ions occupying octahedral sites.

2.1. Magnetic anneal

Magnetic resonance measurements of pure YIG indicated that the magnetocrystalline anisotropy of YIG was small, the first order anisotropy constant, K_1, having a negative value and the second order constant, K_2, having a negligible value. Both values are independent of the frequency of measurement. This result is expected in view of the S-state ground level of the Fe^{3+} ($3d^5$) ions. The magnetic properties become more complicated, however, when ferrous ions are introduced into the samples. At temperatures above about 100K silicon-doped samples exhibit cubic anisotropy when studied using a torque magnetometer ($\vec{M}_s$ being rotated at about one revolution per minute) whilst results from magnetic resonance measurements (angular rotation $\omega \sim 10^{11}$ rad/s) yield an extra component of magnetic anisotropy which is not cubic. The appearance of the non-cubic anisotropy term is attributed to the presence of the ferrous ions. These ferrous ions are able to redistribute themselves, as the magnetization rotates, among the inequivalent octahedral sites by means of a thermally activated valence exchange mechanism. The relaxation time, τ, for the population redistribution is short compared with the rotation period of the torque magnetometer, so that the ferrous ions have time to attain their thermal equilibrium distribution. However, for a magnetic resonance measurement the relaxation time $\tau > \omega^{-1}$. As the temperature of measurement decreases, τ increases and torque curves become dependent upon the rate of rotation of $\vec{M}_s$. Also, when a sample of

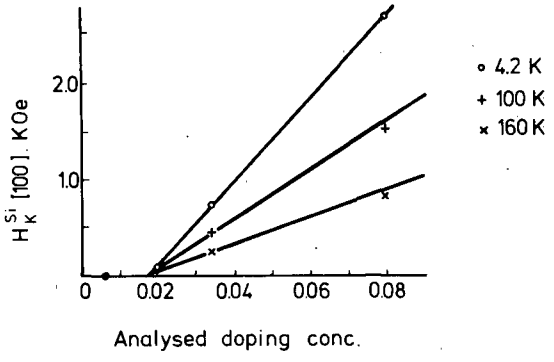

FIG.2.1. The anisotropy field H_K^{Si} [100] introduced into YIG by doping with silicon. The magnetization is along [100]; x gives the silicon doping in the formula $Y_3Fe_{5-x}Si_xO_{12}$. (From Ref.[2.1].)

YIG:Si is cooled to low temperatures and $\vec{M}_s$ is rotated away from the direction along which it was held during cooling, then the observed resonance field or torque is observed to relax to a new value. The new value towards which the resonance field $\vec{H}$ decays is observed to be greater than that which is expected upon cooling the sample with $\vec{M}_s$ in the direction to which rotation has taken place.

These so-called magnetic anneal effects are assumed to be due to ferrous ions being trapped on certain octahedral sites at low temperatures. When $\vec{M}_s$ is rotated into a new direction in the crystal, the equilibrium distribution of the ferrous ions is different from the distribution preferred before the rotation. At low temperatures the energy barrier for valence exchange is greater than the thermal energy, so that the preferred distribution cannot be attained. The valence exchange processes that are still able to take place do so with a spread in relaxation times, and this spread gives rise to a logarithmic decay of the resonance field and torque.

After these general remarks on the influence of Fe^{2+} ions on the anisotropy of YIG, we will investigate the concentration dependence of the induced anisotropy. Figure 2.1 shows the anisotropy field introduced into YIG by doping with increasing amounts of silicon [2.1]. The quantity x gives the analysed amount of silicon in single crystals of $Y_3Fe_{5-x}Si_xO_{12}$. Each specimen was cooled from 300K to 2K with $\vec{M}_s$ fixed along the crystallographic [001] direction. The resonant field H_r was measured at 9.415 GHz during cooling. The difference between the resonant fields for pure and doped specimens, H_K^{Si} [001], is plotted in the figure. It is assumed that the resonant condition at frequency ω is given by

$$H_r = \frac{\omega}{\gamma} - H_K \qquad (2.1)$$

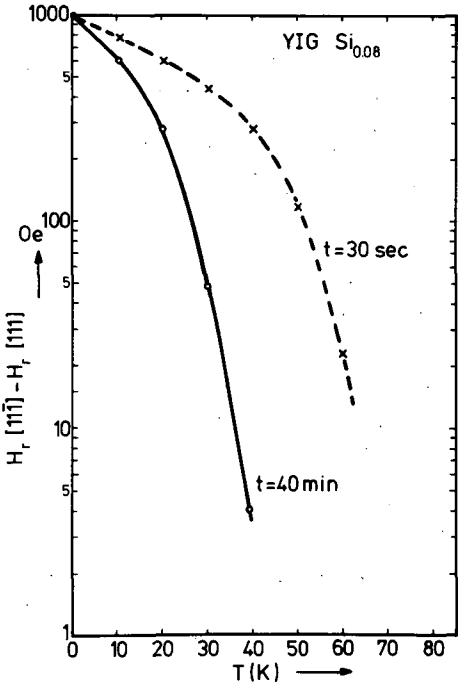

FIG.2.2. $H_r[11\bar{1}] - H_r[111]$ for YIG: $Si_{0.08}$ measured after cooling to T K with magnetization M along [111]. $H_r[11\bar{1}]$ measured after rotating M from [111] to $[11\bar{1}]$ at time t = 0 and T K. Dotted curve for $H_r[11\bar{1}]$ at t = 30 s; full curve at t = 40 min. Measurement frequency 9.43 GHz. (From: TEALE, R.W., TEMPLE, D.W., ENZ, U., PEARSON, R.F., J. Appl. Phys. **40** *(1969) 1435.)*

For silicon concentrations $x < 0.02$ no contribution to the resonant field is observed, i.e. for $0 \leqslant x \leqslant 0.02$ the silicon doping introduces no Fe^{2+}. However, according to the figure, for $x > 0.02$ each Si^{4+} induces one Fe^{2+}. Chemical analysis of the samples indicates the presence of 0.02 atoms of Pb^{2+} per formula unit, which is about the amount required to compensate Si^{4+}. The lead impurities are due to the lead oxide – lead fluoride mixture from which the crystals are grown.

Magnetic anneal effects were studied by cooling each specimen from room temperature to the temperature of measurement with $\vec{M}_s$ held in the [111] direction and then rotating the sample so that $\vec{M}_s$ lay along the $[11\bar{1}]$ direction. The difference between the anisotropy fields in these directions is shown in Fig.2.2. Since [111] and $[11\bar{1}]$ are crystallographically equivalent, the difference arises from the noncubic contribution, which is partly frozen in during cooling. The dotted curve refers to a time 30 s after rotation of $\vec{M}_s$ to $[11\bar{1}]$ and the full curve to 40 min after this rotation.

2.2. An ionic model for the anisotropy

The model adopted is the "single-ion" model [2.2]. The difference between the anisotropy of pure YIG and of YIG:Si is attributed entirely to the anisotropy of the Fe^{2+} ions on octahedral sites. The energy levels, ϵ_i, of these Fe^{2+} ions are determined by the free ion ground state energy and the interactions with neighbouring ions, and are dependent upon the orientation of $\vec{M}_s$ in the crystal. The total anisotropy energy is given by

$$E = \sum_j \sum_i \epsilon_i N_i \tag{2.2}$$

The summation j is over all the different types of the anisotropic ion, type j possessing energy levels ϵ_j of which N_i per volume unit are occupied. In the case of Fe^{2+} in YIG there are four different octahedral sites which we label j = 1,2,3,4. Each type has a trigonal crystal field axis along one of the four body diagonals of the cubic unit cell, e.g. [111], [11$\bar{1}$], [$\bar{1}$11], [1$\bar{1}$1]. The anisotropy energy is due to the coupling of the spins to this local symmetry axis, via the spin-orbit energy $\lambda \vec{L}.\vec{S}$. Hartwick and Smit [2.3] have developed a model which gives a ground state doublet energy of the form

$$\epsilon_j^{\pm} = \pm 2\lambda (\cos^2 \theta_j + f^2)^{1/2} + \Delta \tag{2.3}$$

where λ is the spin-orbit coupling constant and f^2 is a term arising from crystal fields of symmetry lower than trigonal, which are due to the coulombic attraction of a Si^{4+} ion. The angle θ_j is the angle between $\vec{M}_s$ and the trigonal axis of type j. The term Δ has an electrostatic origin due to the disordered distribution of Si^{4+} and Fe^{2+} ions and is in effect an energy zero shift which varies from site to site throughout the lattice. Often Δ is referred to as disorder potential.

With a knowledge of ϵ_j the anisotropy energy can be evaluated and hence the anisotropy field. Another expression often used for the one-ion anisotropy energy is:

$$\epsilon_j = -\epsilon \cos^2 \theta_j$$

where again θ_j is the angle between the local trigonal axis of site j and the magnetization. For YIG the value of ϵ is assumed to be $\epsilon \approx 50$ cm^{-1}.

Let us consider the energy levels as given by Eq.(2.3). The doublet levels for the four types of Fe^{2+} ions are shown in Fig.2.3 as a function of the orientation of the magnetization $\vec{M}_s$ in the (1$\bar{1}$0) plane. We see that if $\vec{M}_s$ is held along [001], then in thermal equilibrium all the four types of octahedral

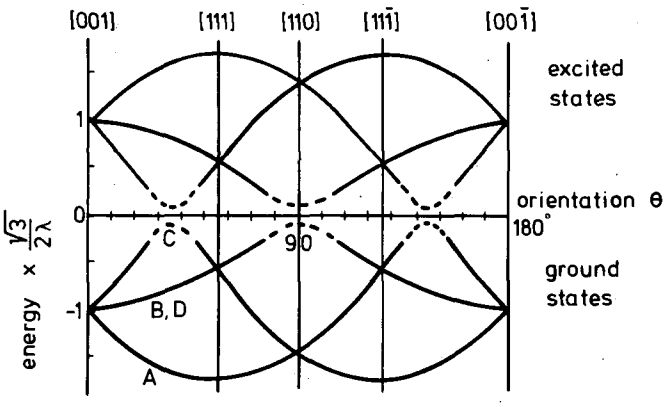

FIG.2.3. Variation of Fe^{2+} doublet energy levels with angle θ in a (1$\bar{1}$0) plane. A and C indicate octahedral sites with a local trigonal axis in the (1$\bar{1}$0) plane, B and D are octahedral sites with trigonal axes in a (110) plane. (From Ref.[2.3].)

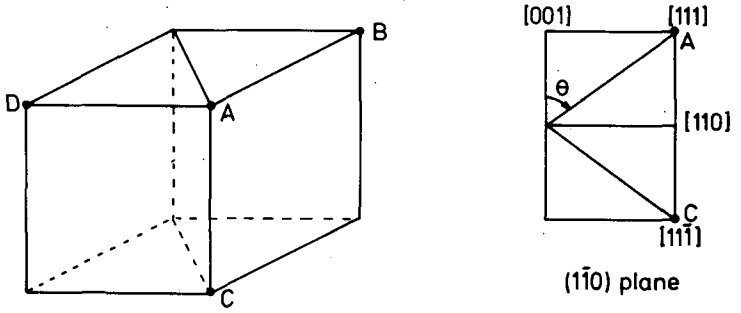

FIG.2.4. Relative positions of the octahedral sites. The local trigonal axes are: [111] for site A, [$\bar{1}$11] for site B, [11$\bar{1}$] for site C, and [1$\bar{1}$1] for site D.

sites should be equally populated with Fe^{2+} ions, since an Fe^{2+} ion would have the same energy on any of the four types of sites. So all N_j should be equal to 1/4N, where N is the total ferrous ion concentration. Ignoring the effect of the term Δ, if $\vec{M}_s$ is held in the [111] direction at $\theta = 54.7°$, then sites having this direction as a trigonal axis (sites of type A) should be preferentially populated, whilst if $\vec{M}_s$ is held in the [110] direction, sites of type A and C should be equally populated, with sites of type B and D being energetically unfavoured (Fig.2.4).

Using the measured Fe^{2+} concentrations Teale et al. calculated the contribution per Fe^{2+} ion per cm^3 to H_K [001] at 4.2K to be 1.12×10^{-17} Oe cm^{-3} per ion, $f^2 = 0.73$ and $\lambda = 51\ cm^{-1}$. To calculate the anisotropy field with $\vec{M}_s$ along any direction other than [001] a knowledge of the distribution of the ferrous ions between the four types of sites is necessary. The first

difficulty is that the Δ values are unknown. At low temperatures there is a further complication since thermal equilibrium is not attained in the experiments.

Teale et al. [2.1] made the following simple estimation of the anisotropy fields. Assume that after cooling to 4.2K with $\vec{M}_s$ along [111] a fraction E of the total ferrous ion content occupies the sites with [111] as trigonal axis. If X_1 is the anisotropy field per Fe^{2+} ion per cm^3 for an Fe^{2+} ion on a site with trigonal axis along [111], and X_2 is the anisotropy field for a ferrous ion on any one of the other three types of sites, then

$$H_K\,[111] = ENX_1 + (1 - E)NX_2$$

From the expression for the resonant field, together with the λ and f^2 values quoted above, they found $X_1 = 0.775 \times 10^{-16}$ Oe $\cdot$ cm^{-3}/ion, $X_2 = -0.306 \times 20^{-16}$ Oe $\cdot$ cm^{-3}/ion, and $E \approx 0.35$. E differs from unity because of the term Δ in Eq.(2.3)! From the observed large deviation we can conclude that Δ is of the same order of magnitude as 2λ, i.e. $\Delta \approx 100$ cm^{-1}. Further they calculated that if $\vec{M}_s$ was rotated from the [111] direction to the $[11\bar{1}]$ direction, a fraction K of the Fe^{2+} ions occupying each type of site after cooling was effectively frozen into the occupied site. The remaining fraction $(1 - K)$ was available for redistribution among the octahedral sites by the thermally activated exchange mechanism. From the measured values of the resonant field at 4.2K with $\vec{M}_s$ in the $[11\bar{1}]$ direction, five minutes after rotation of $\vec{M}_s$ from the [111] direction, they deduced $K \sim 0.25$.

REFERENCES TO SECTION 2

[2.1] TEALE, R.W., TEMPLE, D.W., WEATHERLEY, D.I., J. Phys., C (London) **3** (1970) 1376.
[2.2] WOLF, W.P., Phys. Rev. **108** (1957) 1152.
[2.3] HARTWICK, T.S., SMIT, J., J. Appl. Phys. **40** (1969) 3995.

3. OPTICAL ABSORPTION

In this section we shall deal briefly with the optical absorption properties of the ferrites. Since the spectra of spinel ferrites are closely related to those of the garnets we shall concentrate our attention on YIG.

The garnets are transparent in the infrared region of the spectrum, between approximately 10 000 cm^{-1} (1.24 eV) and 2000 cm^{-1} (0.25 eV). The absorp-

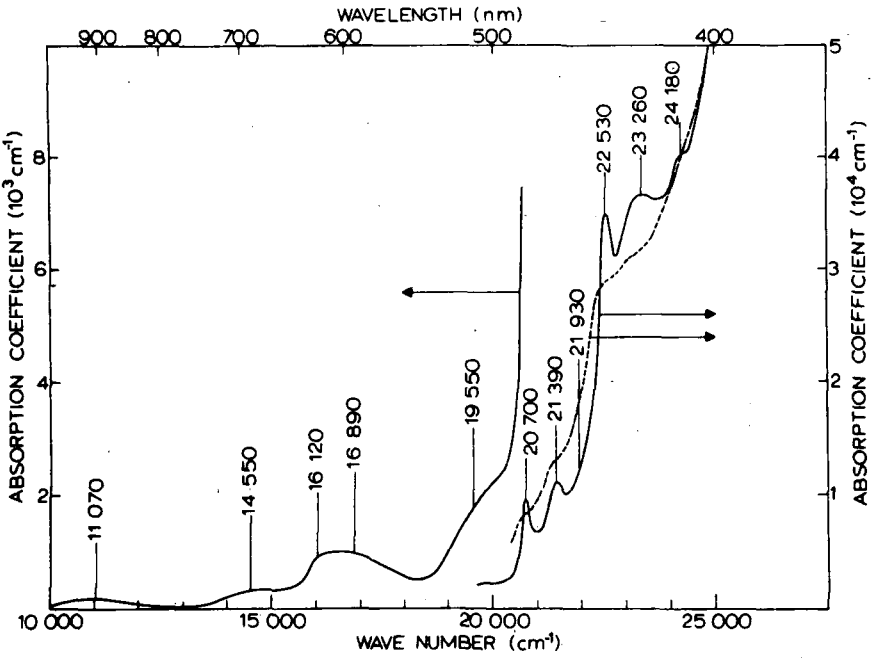

FIG.3.1. Absorption spectrum of $Y_3Fe_5O_{12}$ at 77K (solid line) and 300K (dashed line). The curves were corrected for reflection losses. (From Ref.[3.1].)

tion on the long wavelength wide of this region is due to vibrations of the ions in the unit cell of the crystal. We shall not discuss this region.

On the short wavelength side of the transparent region, the absorption coefficient rises rapidly because of electronic transitions in the trivalent iron ions. Figure 3.1 gives the absorption spectrum in the near infrared and visible region [3.1]. The spectrum is very complicated, and it has been the subject of many investigations. There are two types of transition involved in the absorption. First, there are discrete lines due to crystal field transitions of the ferric ions in the tetrahedral and octahedral sites in the lattice. Secondly, there are absorptions due to charge transfer excitons involving tetrahedral and octahedral iron in the Fe(d)–O–Fe(a) complex.

The crystal field transitions can be assigned in the following way. The free-ion energy levels of the $3d^5$ configuration are used as a starting point. These levels are split by the crystalline fields of O_h and T_d symmetry. The crystal field parameters are chosen to obtain the best fit with the experimentally observed transitions. Such a crystal field fit is shown in Fig.3.2. [3.1]. Using this empirical method the absorption peaks in the region 10 000 – 22 000 cm^{-1} (1.2 eV – 2.7 eV) are assigned to crystal field transitions

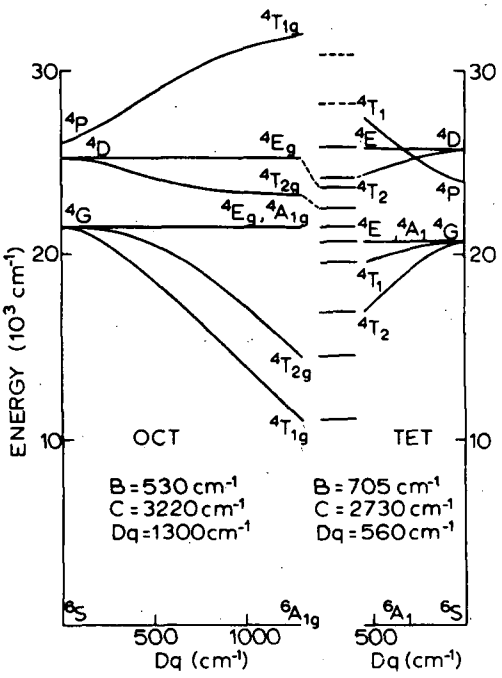

FIG.3.2. Crystal-field fit to the absorption spectrum for tetrahedral and octahedral Fe^{3+} in YIG (From Ref.[3.1].)

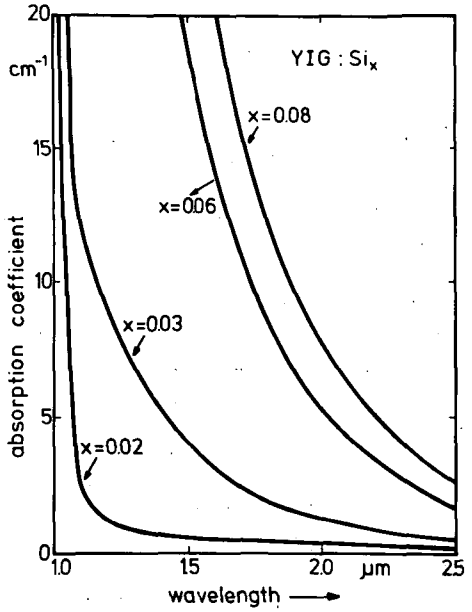

FIG.3.3. Influence of silicon doping on the absorption coefficient of $Y_3Fe_{5-x}\ Si_xO_{12}$.

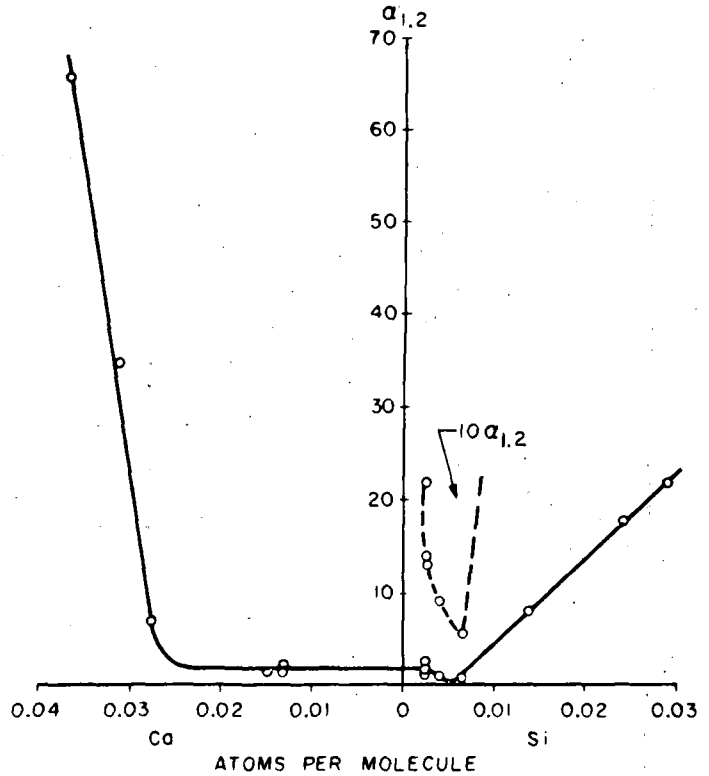

FIG.3.4. Absorption coefficient at 1.2 μm for YIG crystals containing various amounts of Si or Ca. (From Ref.[3.2].)

from the ^6S ground state to excited states of octahedrally and tetrahedrally coordinated iron ions. At higher energies crystal field peaks are superposed on strong charge transition peaks which start at about 23 000 cm^{-1} (2.9 eV). Doping of YIG with Si or Ca produces an increased absorption near the edge at 10 000 cm^{-1} (Fig.3.3). The absorption constant increases over a large spectral region and no discrete absorption peak results when the dopant concentration is increased. The influence of the impurity concentration at a fixed wavelength is shown in Fig.3.4. [3.2]. In the most naive picture the addition of Si^{4+} is considered to produce Fe^{2+} ions, and the addition of Ca^{2+} to produce Fe^{4+} ions in the crystal. From Fig.3.4 it can be seen that the absorption constant at a fixed wavelength can be used as a convenient method to determine the silicon content of a single crystal.

REFERENCES TO SECTION 3

[3.1] SCOTT, G.B., LACKLISON, D.E., PAGE, J.L., Phys.Rev., B. **10** (1974) 971.

[3.2] NASSAU, K., J. Cryst. Growth 2 (1968) 215.

4. PHOTOINDUCED EFFECTS

4.1. Introduction

In 1967 it was found that the magnetocrystalline anisotropy of silicon-doped YIG varies under irradiation with infrared light [4.1]. Shortly afterwards many other observations of photoinduced changes in magnetic properties were reported in the literature. The properties that are light-sensitive include susceptibility [4.2], coercive force [4.2], static magnetic anisotropy [4.3] (measured by means of a torque magnetometer), high frequency anisotropy [4.1] (measured at microwave frequencies) and switching properties [4.4]. Apart from the effects on magnetic properties there are also changes in strain [4.5], in absorption coefficient [4.6] and in linear dichroism [4.7]. The materials known so far to exhibit photoinduced effect are: $Y_3Fe_5O_{12}$ with various dopes; spinel ferrites like $Li_{0.5}Fe_{2.5}O_4$: Ru [4.8], $(NiZn)_1Fe_2O_4$:Co [4.8, 4.9], which are all ferrimagnetic compounds; a ferromagnetic chalcogenide with spinel structure $CdCr_2Se_4$: Ga [4.10]; $FeBO_3$ with various dopes [4.11] (this is an antiferromagnet with slightly canted spins). In our lectures the discussion will be restricted to the garnets and spinel ferrites.

The effects to be discussed are observed well below room temperature. The electrical resistivity of the ferrites is very high in this temperature region owing to the very low mobility of the charge carriers. The electrical behaviour is described with the aid of the small polaron model, i.e. the charge carriers are thought to be localized. In the materials that exhibit photomagnetic effects there are always ions present that can assume different valencies. In silicon-doped iron garnets, for instance, the charge is compensated by Fe^{2+} ions. An electron transport from an Fe^{2+} ion to an arbitrary Fe^{3+} ion in the lattice is equivalent to a displacement of the Fe^{2+} ion to that site. If the two positions of the ferrous ion are inequivalent, e.g. with respect to the local symmetry or with respect to neighbouring ions, they may be expected to give different contributions to the magnetic properties. The physical mechanism common to all photomagnetic effects consists in photoinduced transitions of electrons between cations on different lattice sites, resulting in a redistribution of magnetic ions or centres and thus modifying the magnetic properties. At low temperatures, the photoinduced changes are persistent, due to the low mobility of the electrons; at higher temperatures a competition occurs between photoinduced transitions and thermal electron motion.

Two groups of observations can be distinguished. In section 4.2 light-induced changes observable in saturating magnetic fields are described. These changes are classified as class I photomagnetic effects. Class II photo-

magnetic effects comprise all photoinduced changes that occur regardless of the prevailing magnetization distribution. Class II effects are discussed in section 4.3.

4.2. Photoinduced changes in uniformly magnetized samples

4.2.1. Ferromagnetic resonance experiment

In 1967 Teale and Temple at Sheffield University discovered the photomagnetic effect in a silicon-doped YIG crystal [4.1]. The sample was cooled in the dark from room temperature to 20K, the magnetization being kept in the [111] direction by a high external field. The magnetization is stabilized in this direction by the annealing process described in section 2.1 and the electron distribution is partially frozen in. As expressed in Eq.(2.1) the application of an r.f. field at a fixed frequency ω_r leads to ferromagnetic resonance when the condition

$$H_1 = \omega_r/\gamma - H[111] \tag{4.1}$$

is fulfilled. H[111] is the anisotropy field in the [111] direction. The external field is then turned into the $[11\bar{1}]$ direction, and the magnetization with it. Ferromagnetic resonance now occurs at a field H_2 such that

$$H_2 = \omega_r/\gamma - H[11\bar{1}] \tag{4.2}$$

It turns out that $H_2 > H_1$, or $H[11\bar{1}] < H[111]$, showing that the new direction is less stabilized than the old one. H_2 slowly relaxes to a lower value, still well above H_1. Figure 4.1 shows the experimental values of the resonance field H_2 at 9.4 GHz. Curve A shows the relaxation at 20K. Now upon irradiation with infrared light a reduction of the field H_2 to a value just below H_1 is observed. This shows that irradiation stabilizes the magnetization in the $[11\bar{1}]$ direction to roughly the same extent as it was before in the [111] direction. The change in the anisotropy field $H[11\bar{1}]$ obtained in this way depends on temperature. At 66K the change is 21 Oe, at 20K 130 Oe and at 4.2K a change of 200 Oe is observed.

4.2.2. Torque measurements

Soon after the discovery of photoinduced changes in the resonance field of silicon doped YIG, static anisotropy measurements were performed on YIG:Si crystals by Pearson et al. at the Mullard Research Laboratories [4.3]. From torque curves they measured directly the static magnetic anisotropy induced by the Fe^{2+} ions, and confirmed that it can be altered

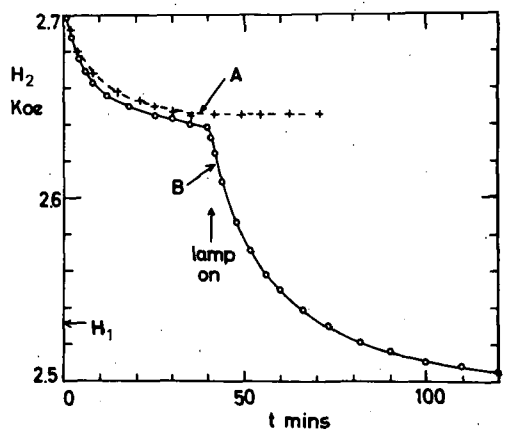

FIG.4.1. Ferromagnetic resonance field H_r plotted against time t, after cooling of the sample with magnetization M along [111] from 300K to 20K, then rotating M to [11$\bar{1}$]. t = 0 when rotation was performed. Frequency 9.4 GHz, sample YIG:$Si_{0.1}$. $0 < t < 40$ min without irradiation, $t > 40$ min during irradiation with a tungsten iodine lamp. (From Ref.[4.1].)

considerably by photon irradiation. They also found that these changes depend on the polarization direction of the incident radiation.

As an example we shall discuss an experiment performed by a group of workers at Bell Research Labs [4.12]. A thin circular disc with the composition $Y_3Fe_{4.97}Si_{0.03}O_{12}$ is cut parallel to a (001) plane. The sample is mounted in a torque magnetometer. The disc can be illuminated by light from a tungsten lamp via a polarizer. The sample is cooled to 4.2K by immersion in liquid helium in a Dewar fitted with a flat window. During cooling a strong magnetic field forces the magnetization along a [100] direction. As follows from the arguments presented in section 2.2 this treatment produces an equal distribution of Fe^{2+} ions over all four inequivalent octahedral sites, as the magnetization direction makes equal angles with the four trigonal axes during cooling. In this initial state no torque is therefore exerted by the field on the sample. At t = 0, the sample is irradiated with an intense beam of white light, incident normal to the surface. With the $\vec{E}$ vector of the light parallel to the [100] direction, the torque remains zero (Fig.4.2). At t = 50 s the polarization is turned parallel to [1$\bar{1}$0]. A positive torque develops and reaches a value of 1.3×10^4 erg/cm^3. At t = 150 the polarization axis is rotated to the [110] axis of the crystal. The positive torque decreases, passes through zero and levels off at a value of -1.3×10^4 erg/cm^3. The torque can be reversed repeatedly between these limits by successive changes of the polarization direction. From this experiment we can conclude that irradiation with $\vec{E}$ along a particular face diagonal makes that direction become a preferred axis.

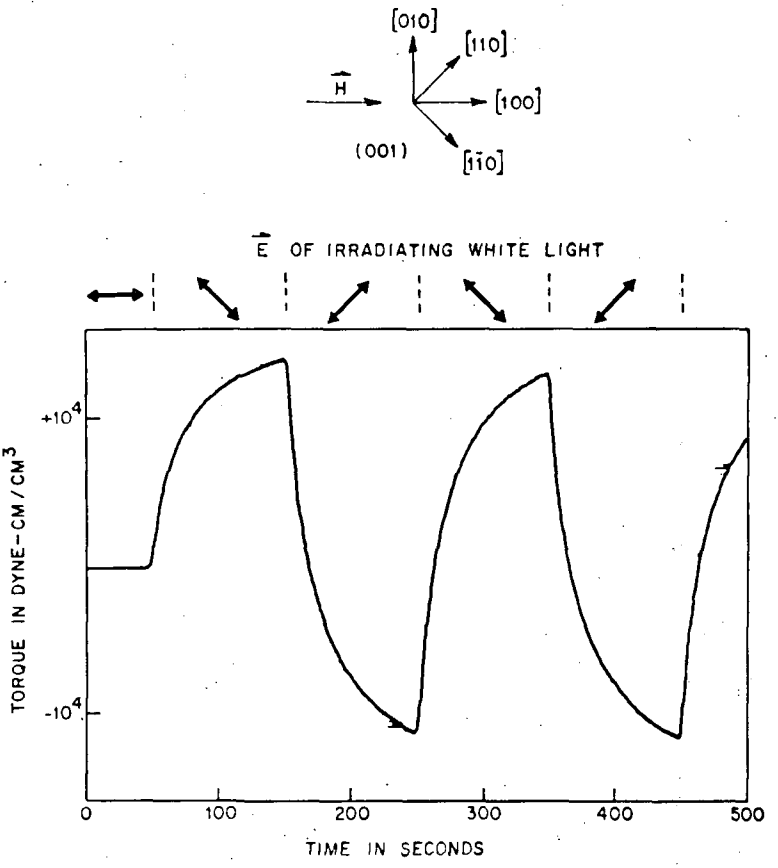

FIG.4.2. Recorder plot of torque about [001] of a YIG:$Si_{0.03}$ crystal at 4.2K on illumination with linearly polarized light. The orientation of the $\vec{E}$ vector shown above the trace may be compared with the crystal axes shown at the top.(From Ref.[4.12].)

4.2.3. Linear dichroism

The magnetic experiments described above can be explained in terms of changes in the occupation numbers of the inequivalent sites. From the torque experiments we have to conclude that absorption of polarized light changes the distribution of the Fe^{2+} ions over the different octahedral sites. However, an anisotropy in the absorption of light implies that there is a dichroism.

When a linear dichroic material transmits a linearly polarized beam the transmitted intensity, $I(\theta)$, is given by

$$I(\theta) = I_{max} \cos^2\theta + I_{min} \sin^2\theta$$

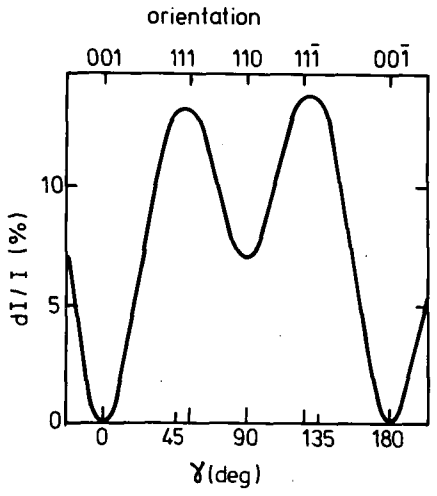

FIG.4.3. The percentage of linear dichroism shown by silicon-doped YIG with magnetization in the (1$\bar{1}$0) plane, as a function of the angle γ between the magnetic field and the [001] direction. The wavelength of the measuring radiation was 1.25 μm and the temperature 70K. (From Ref. [4.13].)

where I_{max} and I_{min} represent the transmitted intensities along the two perpendicular principal axes and θ is the angle between the initial polarization direction and the axis of maximum transmission, which is called the dichroic axis.

For YIG it turns out that the observed dichroism is small. Therefore we put $I_{max} - I_{min} = dI$ and $I_{max} + I_{min} = 2I$. The fractional dichroism dI/I can now be related to the change in absorption coefficient by differentiating the Beer-Lambert law, $I = I_0 \exp(-\alpha t)$, where t is the thickness and α the absorption coefficient. Therefore $dI/It = -d\alpha$ relates the fractional dichroism to the change between $\theta = 0$ and $\pi/2$ in the absorption coefficient.

As expected, Si-doped YIG shows significant dichroism when placed in a saturating magnetic field [4.12, 4.13]. This dichroism is strongly dependent on the orientation of the magnetic field with respect to the crystallographic axes of the sample. Furthermore the dichroism increases when the temperature is lowered. Below 70K relaxation processes are only just noticeable, i.e. upon a rotation of the magnetization at 70K the dichroism reaches a constant value after about 1 second, while at 1.9K at least 10 minutes elapse before equilibrium is obtained. Figure 4.3 shows the percentage dichroism as a function of the angle γ between the magnetic field and the [001] direction in the (1$\bar{1}$0) plane at 70K [4.13]. The wavelength of the light used in the measurements was 1.25 μm, the dichroism was determined with respect to the magnetization $\vec{M}_s$, $d\alpha$ was positive when the polarization direction $\vec{E}$

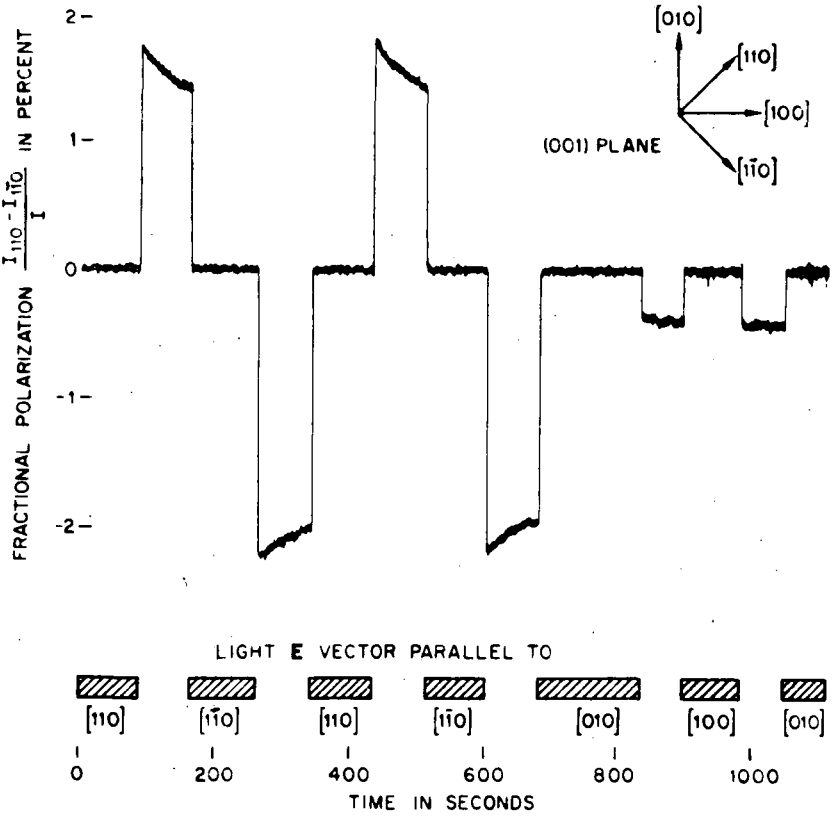

FIG.4.4. Dichroism of a (001) plate of YIG:Si after irradiation with polarized light at 1.5K, with an external field along [100]. The wavelength of the measuring radiation was 1.2 μm. (From Ref.[4.7].)

changed from along $\vec{M}_s$ to perpendicular to $\vec{M}_s$. The form of the dichroism curve can easily be understood from the Hartwick and Smit energy level diagram shown in Fig.2.3. With $\vec{M}_s$ along a [001] direction site populations are equal and there is no resulting dichroism. Maximum dichroism is expected when $\vec{M}_s$ is along a [111] direction.

By analogy with the photoinduced torque, discussed in section 4.2.2, we also expect a photoinduced dichroism. This effect was reported in 1969 by Dillon et al. in a Si-doped (001) YIG platelet [4.7]. After cooling to 1.5K with a saturating field along [100], the plate was irradiated with an intense beam of linearly polarized light. After irradiation the dichroism $(I_{110} - I_{1\bar{1}0})/I$ was measured. The results of this experiment are shown in Fig.4.4. The sample was first irradiated with the $\vec{E}$ vector along [110].

After about 90 s of illumination the dichroism at 1.20 μm approached 2%. After irradiation with light polarized parallel to [1$\bar{1}$0], the dichroism exceeded -2%. Irradiation with $\vec{E}$//[100] led to a dichroism of -0.45%. This corresponds to the slight residual polarization of the original beam.

As will be discussed in more detail in a later section, both photoinduced torque and photoinduced dichroism can be explained if we assume that the photo-detachment cross-section of Fe^{2+} ions depends on the orientation of $\vec{E}$. Finally we remark that a similar explanation holds for the data on light induced strain reported by Dillon et al. [4.5]. Irradiation with $\vec{E}$ normal to [111] produces an elongation along that axis with a relative change in length $\Delta\ell/\ell \sim 10^{-6}$ at 4.2K. This can be ascribed to an excess population of Fe^{2+} on [111] sites, each ion causing a trigonal lattice distortion along its symmetry axis.

So far we have not mentioned the wavelength dependence of the photo-induced effects. The first resonance experiments done by Temple indicated a maximum sensitivity for light with wavelength between about 1 and 2 μm. Measurements of induced linear dichroism confirmed these results. Above about 1.5 – 2.0 μm the sensitivity decreases rapidly since YIG becomes transparent in this region. A maximum sensitivity is observed near 1.0 μm. Below 0.8 μm the sensitivity seems to decrease again. However, accurate sensitivity values are difficult to obtain in this wavelength region owing to the strong increase of the absorption coefficient.

The measurements discussed above were all performed on YIG single crystals doped with silicon (or titanium). The concentration of Fe^{2+} ions necessary to obtain observable photoinduced effects is 0.03 – 0.10 ions per formula unit, i.e. $1 \times 10^{20} - 4 \times 10^{20}$ cm^{-3}. At concentrations below 0.03 the effects of class I disappear, but a new kind of photoinduced effect occurs, which is discussed under the heading "class II effects" in section 4.3.

4.2.4. Phenomenological description of class I photoinduced effects

In order to explain the photoinduced effects observed in silicon-doped YIG it is assumed that photon absorption stimulates valence exchange between iron ions on different types of site. The first step in the transition is the photodetachment, where the photon excites an electron from an iron ion into an excited state. The second step is the electron capture at the same or a different iron site. In the simplest model an equal probability of fall-back to each type of site is assumed [4.14].

It is assumed that the absorption of a photon by a centre destroys the centre. Further it is assumed that a new centre is created after one has been destroyed but the newly created centre has equal probability of possessing each of the four cube diagonals as its preferred axis. If the absorption

probability of the i-th site per unit power of incident radiation is W_i (i = 1,2,3,4), and the total density of Fe^{2+} centres is N, we can write

$$\frac{dN_i}{dt} = -W_i N_i + \frac{1}{4}\sum_i W_i N_i + \frac{N_i^{eq} - N_i}{\tau}$$

If thermal relaxation is ignored the equilibrium population of site i is given by

$$\frac{dN_i^{eq}}{dt} = -W_i N_i + \frac{1}{4}\sum_i W_i N_i = 0$$

This gives

$$N_i^{eq} = N W_i^{-1} / \sum_i W_i^{-1} \tag{4.3}$$

A suitable form for W_i now has to be guessed. Since the trigonal axis is a symmetry axis it seems reasonable to take W_i proportional to $(1 + B\cos^2\alpha_i)$, where α_i is the angle between $\vec{E}$ and the trigonal axis of site i. B is assumed to be constant at a given wavelength and temperature. Similarly effects of the orientation of $\vec{M}_s$ can be accounted for by a term $(1 + C\cos^2\beta_i)$, where β_i is the angle between $\vec{M}_s$ and the trigonal axis of site i. Therefore W_i is assumed to be of the form

$$W_i = A(1 + B\cos^2\alpha_i)(1 + C\cos^2\beta_i) \tag{4.4}$$

where A is a proportionality constant.

With the aid of these equations the experiments discussed in sections 2.1–2.3 can be described. As an example we consider the torque measurements. The octahedral sites 1–4 are situated on the axes [111], [$\bar{1}$11], [1$\bar{1}$1] and [11$\bar{1}$]. We apply a saturating field along [001] and rotate the polarization vector $\vec{E}$ in the (100) plane. ϕ is the angle between $\vec{E}$ and $\vec{M}_s$. We easily find

$$W_1 = W_2 = A[1 + (B/3)(1 + \sin 2\phi)](1 + C/3)$$

$$W_3 = W_4 = A[1 + (B/3)(1 + \sin 2\phi)](1 + C/3)$$

and

$$N_1 = N_2 = \frac{N}{4}\left[1 - \frac{B\sin 2\phi}{(3+B)}\right]$$

$$N_3 = N_4 = \frac{N}{4}\left[1 + \frac{B\sin 2\phi}{(3+B)}\right]$$

If the magnetic field is rotated in the (100) plane a torque $L = -\delta E/\delta\theta$ is exerted by the sample. Here E is the anisotropy energy and θ is the angle made by the magnetization $\vec{M}$ and the [001] reference axis.

In section 2.2 we have seen that the anisotropy energy associated with the Fe^{2+} ions is $\sum_i N_i\epsilon_i$. At low temperatures only the lower level of the ground state doublet of Fe^{2+} is populated and we have $\epsilon_i = -2\lambda(f^2 + \cos^2\theta_i)^{1/2}$. From FMR measurements Teale et al. obtained $f^2 = 0.73$ and $\lambda = 51\ cm^{-1}$. From the known population densities N_i we can calculate the torque $L = -\sum_i N_i(\delta\epsilon_i/\delta\theta)$ for any direction of $\vec{M}_s$ and $\vec{E}$. From the expressions given above we obtain for the torque along the [100] direction, with $\vec{M}_s$ along [001]

$$L = N\frac{2\lambda}{3(f^2 + 1/3)^{1/2}}\ \frac{B \sin 2\phi}{6(1+B/3)}$$

The sin 2ϕ dependence was experimentally verified by Sharp and Teale. If $\vec{M}$ and $\vec{L}$ are chosen along directions of lower symmetry the torque equations also contain C. In this way B and C were evaluated as a function of the Fe^{2+} concentration.

In these calculations thermal relaxation effects have been neglected so far. From the magnetic anneal experiments discussed in section 2.2 we know, however, that thermal relaxation is present. Moreover, the relaxation processes could not be described by a single relaxation time, so that it is rather difficult to include these effects in the model.

Sharp and Teale accounted for the relaxation by replacing N by $N_{eff} = KN$, K being the fraction of sites with lifetimes longer than the time constant of the photoinduced torque change observed during the experiment. This experimental time constant is of the order of minutes, and the corresponding K values are about 0.25. The resulting values of B and C as a function of the Fe^{2+} content are shown in Fig.4.5 [4.14].

The marked fall in the magnitude of B with increased ferrous concentration causes a decrease in the relative sensitivity of the photoinduced torque with increased doping. A similar non-linear dependence of photoinduced dichroism was observed by Gyorgy et al. [4.15].

The dependence of the photoinduced effects on the orientation of the polarization vector is ascribed to the effect of this orientation upon the photodetachment cross-section. The observation that B decreases with increasing dopant concentration means that this dependence of the cross-section on the orientation of $\vec{E}$ becomes less at higher Si concentrations. This may be due to the increase of the low-symmetry distortion of the crystal field at the Fe^{2+} sites, which makes the trigonal axes less dominant. Such low-symmetry distortions were included in a crystal field calculation of the ferrous ion per-

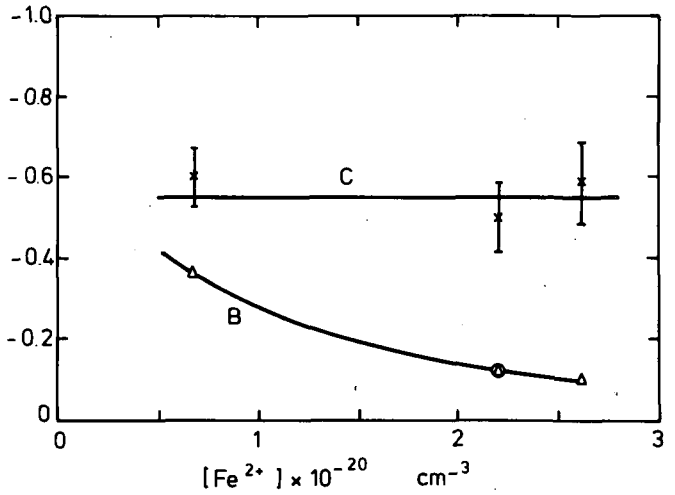

FIG.4.5. Values of B and C (see Eq.(4.4) in the text) against the Fe^{2+} concentration in a YIG: Si sample. (From Ref.[4.14].)

formed by Alben et al. [4.16]. However, these authors concluded that the energy levels of the Fe^{2+} are sensitive to the distortion potential, whereas the photodetachment cross-section is not. This contradicts the interpretation of the silicon dependence of B given by Sharp and Teale. Furthermore the concentration independence of C observed by these authors indicates that the ground state energy of Fe^{2+} is not influenced by the doping concentration. A model that predicts the decrease of B with increasing distortion of the Fe^{2+} site was given by Reik and Schirmer [4.17]. In the next section we shall discuss their results in more detail.

The effect of the orientation of $\vec{E}$ on the photoinduced effects via the photodetachment cross-section seems straightforward. However, the assumption that there is a similar variation of the electron photodetachment cross-section with the orientation of $\vec{M}_s$ seems to be unjustified. Sharp and Teale observed that the time constant for the photomagnetic effects is independent of the orientation of $\vec{M}$. Nevertheless Eq.(4.4) is strongly dependent on the orientation of $\vec{M}_s$ if we substitute $C = -0.55$. Both the experimental data and the theoretical model indicate that the influence of the orientation of $\vec{M}_s$ is due to the unequal capture of photodetached electrons by ions on inequivalent sites. Therefore we have to incorporate unequal capture in the model for W_i. This can be done by replacing W_i in Eq.(4.3) by $W_i^{detach.}/W_i^{capt.}$. Equation (4.4) is then also an expression for $W_i^{detach.}/W_i^{capt.}$, where $W_i^{capt.} = (1 + C \cos^2 \beta_i)^{-1}$.

4.2.5. Microscopic model for class I photoinduced effects

Of the microscopic theories that describe the class I photoinduced effects we shall discuss the model developed by Reik et al. [4.17]. This model, which is based on a polaronic charge transfer between iron ions, gives a straightforward description of both the magnetic and the optical data.

It is assumed that the excitation process consists of an electron transfer from an octahedral to a tetrahedral site. It is further assumed that this electron transport is described by the polaron hopping model. Equilibrium is reached when the number of jumps from octahedral to tetrahedral sites equals the number of jumps in the reverse direction. At low temperatures the transition probability α of octahedral → tetrahedral jumps is given by

$$\alpha^{j,\delta} = \frac{1}{2}\left(\frac{eEd}{\omega}\right)^2 (\vec{a}^{j,\delta}\cdot\vec{e})^2 X(\omega - [\epsilon_t - \epsilon_0^j]) + X(\epsilon_t - \epsilon_0^j)\, e^{-(\epsilon_t - \epsilon_0^j)/kT} \tag{4.5}$$

Here the index j labels the octahedral sites, while δ labels the six tetrahedral sites surrounding each octahedral site. Further, e is the electronic charge, E the amplitude of the electric vector, d the octahedral-tetrahedral distance, ω the frequency of the light, $\vec{a}^{j,\delta}$ is the unit vector pointing from octahedral site j to adjacent tetrahedral site $j+\delta$, $\vec{e}$ is the unit vector in the polarization direction of the incident light, $\epsilon_t - \epsilon_0^j$ is the energy difference of an electron on a tetrahedral site and on the octahedral site with trigonal axis j, and X(x) is the Poisson distribution

$$X(x) = \sqrt{2\pi}\,\eta^{x/\omega_0}\, e^{-\eta}/\Gamma\left(1 + \frac{x}{\omega_0}\right) \tag{4.6}$$

Here η is the average number of phonons in the polaron ($\eta \approx 20$), and ω_0 is the average frequency of the optical phonons in the highest reststrahlen band, $\omega_0 \approx 500\ \mathrm{cm}^{-1}$. The probability γ for tetrahedral → octahedral transitions is written as

$$\gamma^{j,\delta} = X(\epsilon_t - \epsilon_0^j) + \frac{1}{2}\left(\frac{eEd}{\omega}\right)^2 (\vec{a}^{j,\delta}\cdot\vec{e})^2 X(\omega + [\epsilon_t - \epsilon_0^j]) \tag{4.7}$$

It is seen in Eq. (4.5) that the first term describes the light-induced transitions, while the second term represents thermally induced transitions. At liquid helium temperature this thermal contribution can be neglected. The dependence of the photoinduced effects on the polarization direction of the light is fully determined by the geometrical term $(\vec{a}^{j,\delta}\cdot\vec{e})$.

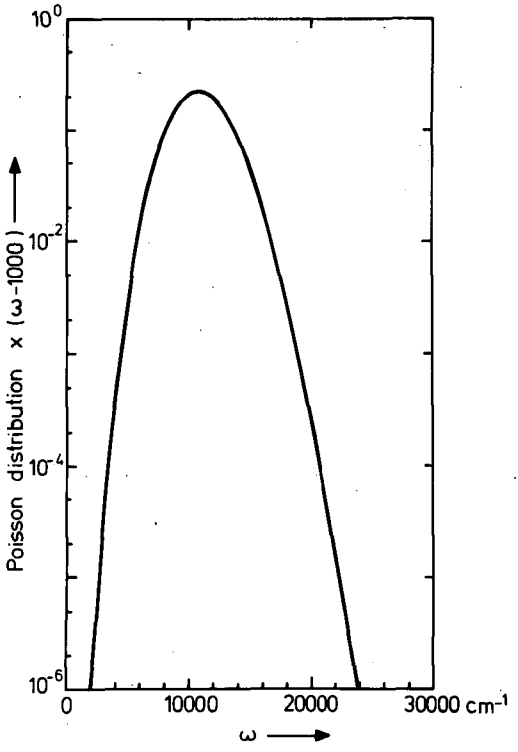

FIG.4.6. The small polaron model predicts a Poisson distribution, X(ω), for the frequency dependence of class I photoinduced effects. The figure shows X (ω − 1000) as a function of the frequency of the light used for excitation:

$$X(\omega - 1000) = 2\pi\,\eta^{(\omega-1000)/\omega_0} e^{-\eta} \Big/ \left(1 + \frac{\omega - 1000}{\omega_0}\right), \text{ with } \eta = 20, \text{ and } \omega_0 = 500\ cm^{-1}.$$

The wavelength dependence of the excitation is described by the Poisson distribution function. A reasonable value for $\epsilon_t - \epsilon_0^j$ is about 10^3 cm^{-1}. The resulting frequency dependence is shown in Fig.4.6.

The rate of fall-back to octahedral sites is determined by Eq.(4.7). Evaluation of this relation shows that the second term can be neglected, so that $\gamma^{j,\delta} = X(\epsilon_t - \epsilon_0^j)$. This means that the fall-back is a random process, independent of the polarization direction. The influence of the magnetization direction is described by the ϵ_0^j, which is present both in the α and γ. However, in the α-term ϵ_0^j occurs as $(\omega - \epsilon_t + \epsilon_0^j)$, and therefore changes in j have hardly any influence when we irradiate with a light frequency close to the maximum of $X(\omega - \epsilon_t + \epsilon_0^j)$, i.e. for $\omega \approx 10^4$ cm^{-1}. From this consideration we see that the magnetization direction only influences the process of fall-back.

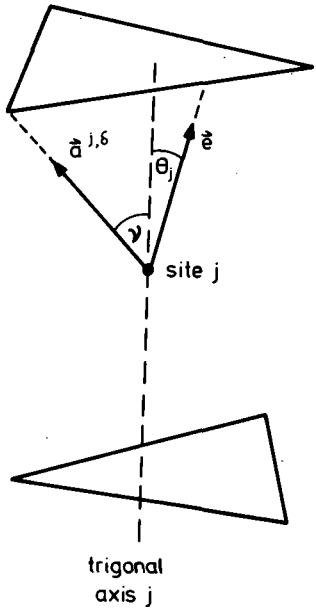

FIG.4.7. Surrounding of an octahedral site j by six tetrahedral sites in the direction $\vec{a}^{j,\delta}$. $\vec{e}$ *is the unit vector in the polarization direction of the incident light.*

When excitation and fall-back are in equilibrium we easily find that the population of the octahedral sites is proportional to

$$\langle n_0^j \rangle_{eq.} \propto \sum_{\delta=1}^{6} (\vec{e}\cdot\vec{a}^{j,\delta})^2 \frac{X(\epsilon_t - \epsilon_0^j)}{X(\omega - [\epsilon_t - \epsilon_0^j])} \tag{4.8}$$

If ν is the angle between the trigonal axis and the vector $\vec{a}^{j,\delta}$, and θ_j is the angle between $\vec{e}$ and the trigonal axis (see Fig.4.7), the geometrical term can be written as $1 - \cos^2\theta_j\,(1 - 2\cot^2\nu)$. So, if we write $B = -1 + 2\cot^2\nu$, we have

$$\sum_{\delta} (\vec{e}\cdot\vec{a}^{j,\delta})^2 \propto (1 + B\cos^2\theta_j)^{-1}$$

which is identical with the relation (4.4) used by Teale et al. If $\vec{a}^{j,\delta}$ is the direction from an octahedral to a tetrahedral site, we calculate $\nu \cong 75°$, so $B = -6/7$, which is about a factor of two higher than the experimental value

given by Sharp and Teale [4.14]. A better agreement is obtained if we assume a distortion of the Fe^{2+} site. For instance a value of $\nu = 60°$ gives $B = -0.4$.

If the single ion energy ϵ_0^j is approximated by the simple form $\epsilon_0^j = \epsilon_0 - \epsilon \cos^2\beta_j$, an expansion of the Poisson distributions in Eq.(4.8) gives the following approximation

$$\langle n_0^j \rangle_{eq.} \propto (1 + B \cos^2\theta_j)^{-1} (1 + C \cos^2\beta_j)^{-1} \tag{4.9}$$

Here β_j is the angle between the trigonal axis and the magnetization direction. Equation (4.9) is equivalent to the phenomenological expression (4.4). The frequency-dependent constant C is given by

$$C = -\frac{\epsilon}{\omega_0}\left\{2\ln\eta - \psi\left(1 + \frac{\omega - \epsilon_t + \epsilon_0}{\omega_0}\right) - \psi\left(1 + \frac{\epsilon_t - \epsilon_0}{\omega_0}\right)\right\}$$

where ψ is the digamma function $\psi(z) = \Gamma'(z)/\Gamma(z)$. For $\epsilon \approx 50\ cm^{-1}$, $C = -0.22$ for $\omega = 10\,000\ cm^{-1}$ and $C = -0.17$ for $\omega = 15\,000\ cm^{-1}$.

The dichroism measurements by Hawkes and Teale [4.13] showed that B is indeed frequency-independent; for C the frequency dependence is unknown.

We can make the following remarks on this theory. The basis of the theory is the small polaron hopping model. Measurements of electrical conductivity, Seebeck coefficient and Hall effect as a function of temperature are as yet indecisive. However, low temperature magnetic data e.g. on magnetic anneal and on photoinduced effects can be explained very well with this theory. The assumption that the excitation of electrons induces a jump from octahedral sites to tetrahedral sites is less certain. If the excitation follows an indirect path, the value of B also changes. It should also be mentioned that the experimental B and C values are subject to considerable uncertainty due to the relaxation processes. The frequency dependence of the photomagnetic effect predicted by this model seems to correspond with the experimental data on class I effects. The shape of the sensitivity curve at the high-frequency side is difficult to measure owing to the increase of the absorption. Measurements on class II effects, to be discussed in the next section, indicate a sensitivity which increases continuously from about $10\,000\ cm^{-1}$ to higher frequencies [4.18].

4.3. Photoinduced effects in low or zero fields

All photoinduced effects of class I, which were discussed in section 4.2, are characterized by anisotropic ferrous ions on lattice sites made inequivalent by the magnetization direction. The photoinduced effects of class II, which

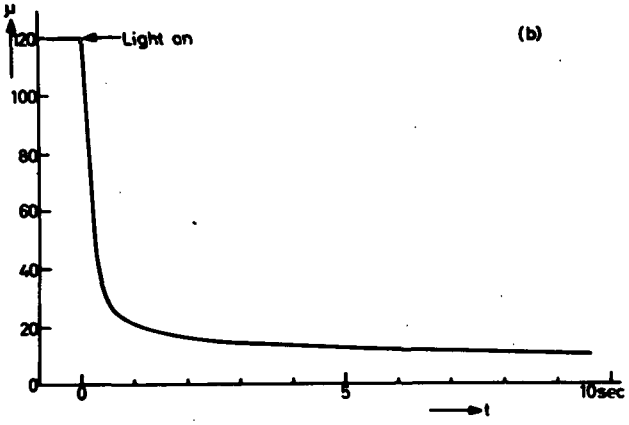

FIG.4.8. Time dependence of the initial permeability of a polycrystalline YIG: $Si_{0.006}$ ring at 77K under irradiation with white light of intensity 0.01 W· cm^{-2}.

are discussed in this section, are independent of the magnetization direction. Therefore these effects cannot be explained by the same kind of site inequivalence.

4.3.1. Changes in susceptibility and coercive force

In 1968 Enz and Van der Heide [4.19] discovered photoinduced changes in the susceptibility and coercive force of a YIG single crystal doped with about 0.02 Si atoms per formula unit. Later similar changes were reported in compounds with different crystal structures and different compositions [4.4, 4.8, 4.9, 4.10]. In these experiments the initial susceptibility is measured on toroidal samples. A small a.c. field is generated by a current through a few primary windings. The induced voltage in a secondary winding is directly proportional to the permeability μ (susceptibility $4\pi\chi = \mu - 1$).

We shall first describe a typical experiment on a YIG: Si sample. The sample is cooled in the dark to 77K. When the specimen is irradiated with light in the wavelength region $0.6 - 1.5$ μm, the permeability drops in a few seconds to a much lower value (Fig.4.8). At temperatures below a certain temperature T_r this change in the permeability is irreversible, that is to say magnetic fields, upon renewed irradiation at the same or different wavelength, have no influence on the low-permeability state. At temperatures above T_r a thermally activated relaxation occurs, which restores the original high-permeability state of the sample. For YIG the critical temperature T_r is about 120–150K. For experiments at $T < T_r$ the magnetization state during irradiation is irrelevant. For instance demagnetization either after or during irradiation

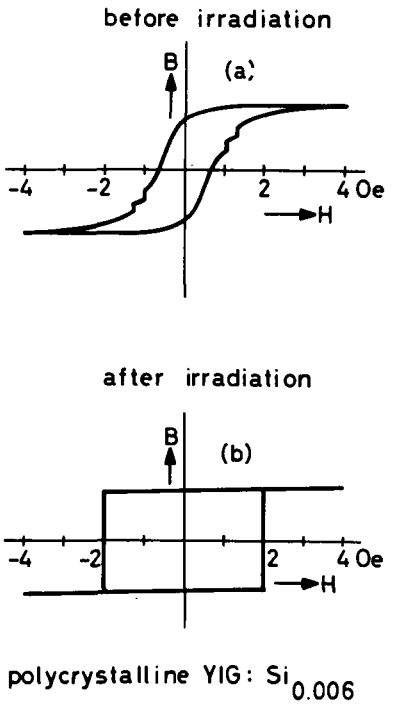

FIG.4.9. Hysteresis loop of polycrystalline YIG: $Si_{0.006}$ at 50 Hz and 77K: (a) after cooling in the dark, (b) after irradiation with white light.

has no influence on the low permeability value; even if the sample is saturated magnetically during irradiation the same permeability value is obtained upon return to the demagnetized state. An important conclusion from these observations is that the change is uniform through the volume of the sample and is not in any way connected with the local magnetization direction during irradiation. These are characteristic properties of class II effects.

As the direction of the magnetization proves not to be involved in this class of photoinduced effects, we are not restricted to the use of single crystals. Indeed strong photomagnetic effects have been observed in polycrystalline YIG samples (Fig.4.8) [4.20].

The coercive force of yttrium iron garnet is also affected by electromagnetic radiation at low temperature. Figure 4.9 shows the change in the hysteresis loop for a polycrystalline ring of YIG: $Si_{0.006}$: the loop becomes square upon irradiation at 77K and H_c increases from 0.6 to 2.0 Oe (7.5 – 25 mA/m). The irregularities in curve a are due to the Barkhausen effect, i.e. the discontinuous displacement of domain walls in a continuously changing external field.

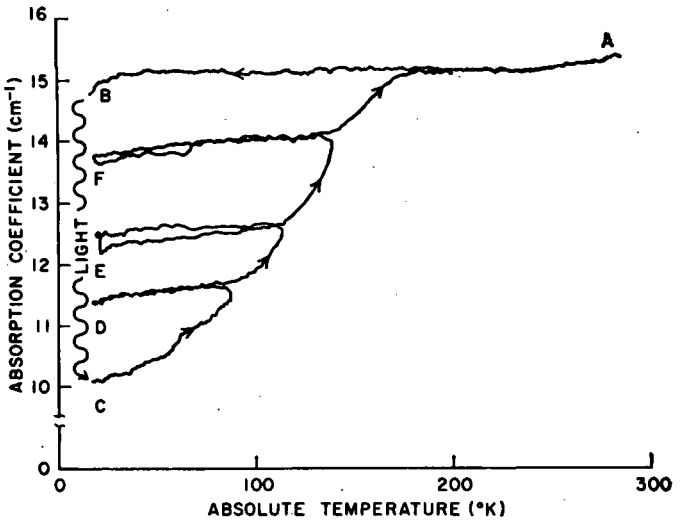

FIG.4.10. The absorption coefficient at 1.15 μm of YIG : Si as a function of temperature. The sample was cooled from A to B and then illuminated. After irradiation the sample was cyclically heated as shown. (From Ref.[4.23].)

This change in the hysteresis properties is even more pronounced when so-called switching measurements are carried out [4.4]. In these experiments we measure the amount of flux switched by a square field pulse of magnitude H and pulse duration τ ($\tau \sim 10-1000$ ns). For further details we refer to the literature [4.4, 4.9, 4.20].

Measurements on spinel ferrites give similar photomagnetic changes in permeability and coercive force [4.8, 4.9, 4.22].

The observed change in permeability depends on the product of light intensity and time. The spectral dependence was studied by measuring the speed of the permeability change at a fixed temperature as a function of the wavelength of the irradiating light. There is a fairly sharp photomagnetic edge situated around 1.2 μm (~ 1.0 eV). At higher wavelengths there is no effect since YIG is transparent in this region. Towards shorter wavelengths there is a strong increase in the sensitivity [4.2, 4.18]. X-rays too are effective [4.19].

4.3.2. Related irreversible photoinduced changes

A careful study of the optical absorption in YIG : Si and YIG : Ca has revealed that the photomagnetic effects are accompanied by changes in absorption constant [4.23]. Figure 4.10 shows the experimental results for a Si-doped YIG sample. The absorption coefficient $\alpha = (1/t)\ln(I_0/I)$ at

1.15 μm is plotted as a function of temperature. The experiment started at room temperature, point A. The sample was then cooled to 20K, point B. After irradiation the absorption constant at 20K proved to have decreased from 15 cm^{-1} to about 10 cm^{-1} (point C). α only started to decrease again when the sample was heated above 100K. The relaxation process was frozen in if, at an intermediate stage, the sample was cooled to 20K again (points D, E).

In Ca-doped YIG a similar irreversible change of α is observed. However, contrary to the YIG:Si case, irradiation causes an increase of the absorption in YIG:Ca.

4.3.3. A model for class II effects

A simple phenomenological model has been proposed by Lems et al. [4.10]. It is assumed that two types of lattice sites occur in the material, called "near" and "far" sites, which can either be occupied or be empty. It is known that the susceptibility of YIG is mainly determined by domain wall contributions (cf. section 1.3.3). The reduction of the susceptibility therefore means that the domain walls are pinned more strongly, in other words the wall stiffness has increased due to the irradiation. Suppose that the centres on near sites, which are relatively few in number, have low energy and low domain wall pinning strength, whereas at the more frequently occurring far sites they have a higher energy and a high pinning strength. The centres move through the lattice by photon-induced electron transport.

More specifically, in silicon-doped YIG near sites are thought to be Fe^{2+} ions on octahedral sites adjacent to the Si^{4+} sites, while far sites are identical with Fe^{2+} ions surrounded by Fe^{3+} ions only, i.e. far from the silicon donors. The action of the light is then simply described by the reaction:

$$\text{Filled near site} + h\nu \leftrightarrows \text{Empty near site} + \text{Occupied far site},$$

or for YIG:Si:

$$Fe^{2+} \cdot Si^{4+} + h\nu \leftrightarrows Fe^{2+} + Si^{4+}$$

Such a dissociation leads to a rate equation of the form

$$dn/dt = -an^2 + bI(n_0 - n) \qquad (4.10)$$

where n is the number of dissociated centres (i.e. occupied far sites), n_0 is the total concentration of centres (i.e. the number of filled near centres at the time $t = 0$) and I is the photon current density. The proportionality constant b is a wavelength-dependent sensitivity, while a is a temperature-dependent relaxation-rate coefficient. The relaxation process is thought to be thermally

activated, with

$$a = a_0 \exp(-E_a/kT)$$

For $t \geqslant 0$ the solution of Eq.(4.10) is

$$n(t) = \frac{2n_0}{1 + z \coth(\frac{1}{2} bIzt)} \tag{4.11}$$

with $z = (1 + 4an_0/bI)^{1/2}$. Under steady state conditions the saturation concentration n_s of the dissociated centres is given by

$$n_s = 2n_0/(1 + z)$$

After the light has been switched off the relaxation is described by

$$n(t) = n_s/(1 + an_s t)$$

In order to describe the experimental results we need a relation between the concentration n and the measured magnetic properties, e.g. the change in coercive force ΔH_c or the change in the inverse susceptibility $\Delta\chi^{-1} = \chi^{-1}_{irr} - \chi^{-1}_{dark}$ (according to Eq.(1.16) $\Delta\chi^{-1}$ is proportional to the change in wall stiffness). According to Lems et al. [4.24] for low concentrations one has simply $\Delta\chi^{-1}$ or ΔH_c proportional to n. For higher concentrations $\Delta\chi^{-1}$ and ΔH_c seem to be more nearly proportional to $n^{1/2}$. The experimental data are found to be in good agreement with this mathematical model [4.4, 4.24].

4.3.4. Microscopic model for class II effects

In this section we shall investigate the two-centre model in more detail. We have indicated already that the effects are attributed to two types of Fe^{2+} ions which differ in their domain wall pinning strength. This direct influence on the domain walls is evident from theoretical considerations, but it can also be demonstrated directly from domain wall observations [4.25]. As indicated in the previous section a distinction between the Fe^{2+} ions can be made by considering the distance with respect to the silicon ions. The Si^{4+} ion has an effective positive charge compared with the neutral lattice which consists of Fe^{3+} ions. An Fe^{2+} on a nearest neighbour site will have a lower energy than on a site far away from the silicon. The corresponding electrostatic energy difference is estimated to be $E = -e^2/\epsilon r \approx 0.2 - 0.4$ eV. This difference is independent of the local magnetization direction. Therefore, after cooling from room temperature to 77K or lower temperatures, we expect that all Fe^{2+}

ions will be in "near sites". During irradiation the electrons are transported through the lattice and are trapped at sites far away from the silicon. This means that we are restricted to low dopant concentrations, since otherwise there are no sites far from silicon. The electric field and the lattice distortion due to the Si^{4+} ion will cause a considerable change in the local symmetry. The magnetic anisotropy of an Fe^{2+} ion, which is caused by the spin-orbit coupling, will be reduced considerably in a low symmetry crystal field.

The movement of a domain wall through the lattice means a rotation of the electron spins in the wall. Such a rotation is impeded if a spin is strongly bound to a certain crystallographic direction, i.e. if there is a strongly anisotropic ion present in the wall. As a result Fe^{2+} ions in far sites will have a higher pinning strength on the domain walls than ions in near sites.

Indeed from careful measurements, Flanders et al. [4.26] confirmed that the cubic anisotropy of YIG : Si changed under irradiation.

Of course, instead of silicon ions all kinds of electron donors can be used. This explains the observation of photomagnetic effects in undoped YIG, since here the role of silicon ions is taken over by oxygen vacancies [4.27]. This qualitative model gives a simple explanation of the experimental results. For instance, the permanence of the effects at low temperatures, the independence of the magnetization direction, and the fact that for higher dopes the class II effects disappear, all follow immediately. On the other hand it is clear that this model is an over-simplification of the real situation. The distinction between near and far sites cannot be as simple as assumed above. This is also evident from experiments. We know, for example, that there is a wide distribution of relaxation times, which means that there is a wide distribution of activation energies for electrons on the octahedral sites.

To account for this fact the model has been extended. Moreover, class I effects are also included in this extended model [4.2]. It is assumed that the barrier height E_b, the absolute value of the ground state energy of the Fe^{2+} ion [the disorder potential Δ in the Hartwick and Smit equation (2.3)] and the one-ion anisotropy energy ϵ all depend on the distance r between the Fe^{2+} and the nearest Si^{4+} ion. Here ϵ is the constant from the empirical expression for the one-ion anisotropy energy, $\epsilon_j = -\epsilon \cos^2 \beta_j$ (cf. section 2.2). Figure 4.11 gives a qualitative picture of the model. It is assumed that the energies vary as 1/r.

In fact, when we measure an anisotropic energy or relaxation time, we obtain an average value of this quantity, weighted with the distribution of ferrous ions over the lattice. For higher dopant concentrations the average will lie at low r values; for increasing temperature, more sites with larger r will be occupied, so high r values will be favoured. The value of Δ gives the electrostatic energy of an Si^{4+}–Fe^{2+} pair, which is of the order of a few tenths of an electron volt for nearest neighbours. At low temperatures all Fe^{2+} ions are expected therefore to be at the shortest possible distance from Si^{4+}. Yet,

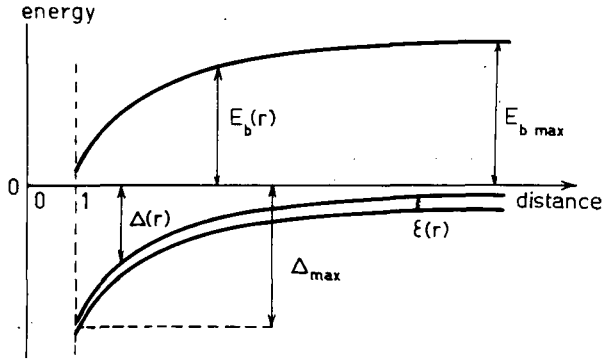

FIG.4.11. Model for Si-doped YIG. Energies as a function of distance from the disturbing Si centre, expressed in units of the $Si^{4+} - Fe^{2+}$ nearest-neighbour distance. Lower curves, ground state energies for ions with trigonal axes parallel or perpendicular to the magnetization, respectively. Upper curve, barrier energy E_b for electron transport between octahedral sites. (From Ref.[4.2].)

at 4.2K the FMR anisotropy measurements revealed an appreciable relaxation [4.1]. This can be explained if the barrier height E_b at the low r side in Fig.4.11 is very small, and probably less than 0.05 eV. This means that in a static (torque) anisotropy measurement the Fe^{2+} ions next to Si^{4+} do not contribute to the light-induced anisotropy at $T > 4K$. We think we can identify these fast relaxing ions with the fraction $(1 - K)$ of ions which do not contribute to the photoinduced processes as described by Teale et al. [4.1, 4.28]. Measurements at higher temperatures give information about the large distance properties. From the relaxation of the susceptibility and coercive force near 200K we estimate the barrier height E_b to be approximately 0.2 eV.

Though it is difficult to use this model quantitatively, it has the merit that it describes all the experimental data on photoinduced effects in a qualitative way. In principle the polaron model proposed by Reik et al. [4.17]. can also be used to describe the class II effects, but this has not yet been carried out.

REFERENCES TO SECTION 4

[4.1] TEALE, R.W., TEMPLE, D.W., Phys. Rev. Lett. **19** (1967) 904.
[4.2] ENZ, U., METSELAAR, R., RIJNIERSE, P.J., J. Phys. (Paris) **32** C1 (1971) 703.
[4.3] PEARSON, R.F., ANNIS, A.D., KOMPFNER, P., Phys. Rev. Lett. **21** (1968) 2805.
[4.4] HOLTWIJK, T., LEMS, W., VERHULST, A.G.H., ENZ, U., IEEE Trans. Magn. MAG–6 (1970) 853.
[4.5] DILLON, J.F., Jr., GYORGY, E.M., REMEIKA, J.P., Appl. Phys. Lett. **15** (1969) 221.

[4.6] DILLON, J.F., Jr., GYORGY, E.M., REMEIKA, J.P., J. Phys. (Paris) **32** C1 (1971) 794.
[4.7] DILLON, J.F., Jr., GYORGY, E.M., REMEIKA, J.P., Phys. Rev. Lett. **22** (1969) 643.
[4.8] JONKER, H.D., J. Solid State Chem. **10** (1974) 116.
[4.9] METSELAAR, R., HUYBERTS, M.A.H., Philips Res. Rep. **29** (1974) 453.
[4.10] LEMS, W., RIJNIERSE, P.J., BONGERS, P.F., ENZ, U., Phys. Rev. Lett. **24** (1968) 1643.
[4.11] LACKLISON, D.E., CHADWICK, J., PAGE, J.L., J. Phys., D. (London) **5** (1972) 810.
[4.12] DILLON, J.F., Jr., GYORGY, E.M., REMEIKA, J.P., J. Appl. Phys. **41** (1970) 1211.
[4.13] HAWKES, J.F.B. , TEALE, R.W., J. Phys., C. (London) **5** (1972) 481.
[4.14] SHARP, B.T., TEALE, R.W., J. Phys., C (London) **7** (1974) 965.
[4.15] GYORGY, E.M., DILLON, J.F., Jr., REMEIKA, J.P., IBM J. Res. Dev. **14** (1970) 321.
[4.16] ALBEN, R., GYORGY, E.M., DILLON, J.F., Jr., REMEIKA, J.P., Phys. Rev. **B5** (1972) 2560.
[4.17] REIK, H.G., SCHIRMER, R., Solid State Commun. **10** (1972) 1209.
[4.18] METSELAAR, R., HUYBERTS, M.A.W., LOGMANS, H., J. Appl. Phys. **46** (1975) 3171.
[4.19] ENZ, U., VAN DER HEIDE, H., Solid State Commun. **6** (1968) 343.
[4.20] ENZ, U., LEMS, W., METSELAAR, R., RIJNIERSE, P.J., TEALE, R.W., IEEE Trans. Magn. MAG-5 (1969) 467.
[4.21] VERHULST, A.G.H., HOLTWIJK, T., LEMS, W., ENZ, U., IEEE Trans. Magn. MAG-7 (1971) 729.
[4.22] MARAIS, A., MERCERON, T., Phys. Status Solidi **A22** (1974) K209.
[4.23] GYORGY, E.M., DILLON, J.F., Jr., REMEIKA, J.P., J. Appl. Phys. **42** (1971) 1454.
[4.24] LEMS, W., METSELAAR, R., RIJNIERSE, P.J., ENZ, U., J. Appl. Phys. **41** (1970) 1248.
[4.25] HAISMA, J., ROBERTSON, J.M., ENZ, U., Solid State Commun. **10** (1972) 1021.
[4.26] FLANDERS, P.J., GRAHAM, C.D., Jr., DILLON, J.F., Jr., GYORGY, E.M., REMEIKA, J.P., J. Appl. Phys. **42** (1971) 1443.
[4.27] METSELAAR, R., HUYBERTS, M.A., J. Phys. Chem. Solids **34** (1973) 2257.
[4.28] TEALE, R., TEMPLE, D.W., WEATHERLEY, D.I., J. Phys., C. (London) **3** (1970) 1376.

5. MAGNETO-OPTIC EFFECTS

5.1. Introduction

In the preceding section we have dealt with the influence of electromagnetic radiation on the magnetic properties of ferrites. These phenomena are known under the name of photomagnetic effects. We have also investigated photoinduced changes in physical properties such as strain and absorption constants, which are influenced by the same mechanism. In this section

we shall investigate the magneto-optical behaviour of the ferrites. This is in a sense the reverse effect, being the influence of the internal magnetization on the electromagnetic radiation. However, photoinduced effects are caused by the presence of point defects, whereas magneto-optic effects are caused by the magnetization, which is a bulk property of the solid.

Interest in the magneto-optical properties of magnetic materials has grown very rapidly because of the possible application of these effects in devices. Devices working at optical frequencies are of particular interest for use as modulators, rotators and magneto-optical memories. These devices employ Faraday rotation, i.e. the rotation of the plane of polarization of a linearly polarized light beam passing through the magnetized crystal. However, in this lecture the emphasis will not be on devices, but on understanding the origin of the effects. The first step in our discussion will be to investigate the relation between the observable quantities and the dielectric tensor elements. Next we shall relate this tensor to microscopic material parameters such as energy level separation and transition probabilities. These two parts are based on the excellent review articles by Freiser [5.1] and Suits [5.2]. Finally some examples of magneto-optic spectra will be given.

5.2. Magneto-optic observables

We shall describe polarized light by means of the electric field $\vec{E}$. In circularly polarized light, $\vec{E}$ rotates in the plane perpendicular to the direction of propagation. We use the definition that light is right-circularly polarized (RCP) if, when one looks against the direction of propagation, the $\vec{E}$ vector rotates clockwise. Circular polarization and linear polarization are special cases of elliptical polarization. Thus, if δ is the phase difference between the x and y components of a wave propagating in the positive z direction of a cubic crystal, then

$$\vec{E} = \frac{1}{2} E_0 (\vec{e}_x + e^{i\delta} \vec{e}_y) \exp[i(\omega t - kz)] + \text{c.c.} \qquad (5.1)$$

Here c.c. stands for complex conjugate, and $\vec{e}_x$ and $\vec{e}_y$ are unit vectors along the positive x and y axes respectively. For $\delta = 0$, Eq.(5.1) represents a linearly polarized wave; for $\delta = \pi/2$ we have an RCP wave.

If linearly polarized light passes through a material which is placed inside a magnetic field, the transmitted light can show four different effects.

(1) We shall first discuss the properties of a linearly polarized wave propagating in the positive z direction: $\vec{k} \parallel \vec{H} \parallel z$. Due to the magnetization the medium shows birefringence, i.e. the refractive indices n_+ and n_- for RCP and LCP light will be different. If at the point $z = 0$ the wave is linearly polarized along the x direction, then in the medium the wave is given by:

$$\vec{E} = \frac{1}{2} E_0 \{(\vec{e}_x + i\vec{e}_y)\exp[i(\omega t - 2\pi n_+ z/\lambda_0)] + (\vec{e}_x - i\vec{e}_y)\exp[i(\omega t - 2\pi n_- z/\lambda_0)]\}$$

$$= E_0\left(\vec{e}_x \cos\frac{\Delta}{2} + \vec{e}_y \sin\frac{\Delta}{2}\right)\exp[i(\omega t - 2\pi n_0 z/\lambda_0)] + \text{c.c.} \qquad (5.2)$$

Here $n_0 = \frac{1}{2}(n_+ + n_-)$, $\Delta = 2\pi z(n_+ - n_-)/\lambda_0$, and λ_0 is the wavelength in vacuum.

Equation (5.2) describes a linearly polarized wave with its direction of polarization turned through an angle $\Delta/2$ from the x direction toward the y direction. This rotation of the polarization direction, which is due to the birefringence produced by a magnetic field, is called Faraday rotation θ_F or magnetic circular birefringence (MCB). θ_F is the Faraday rotation per unit thickness of the sample. In paramagnetic materials the magnetization is proportional to the applied field, and consequently the rotation is proportional to the applied magnetic field: $\theta_F = VH$. The material constant V is the Verdet constant. In our case of ferrimagnetic materials the external magnetic field is used only for magnetic saturation of the sample. In this case, the magneto-optic effects depend on the saturation magnetization $\vec{M}$, rather than on the applied field. If the medium is absorptive, n is a complex quantity:

$$n_\pm = N_\pm - iK_\pm \qquad (5.3)$$

where N and K are real quantities, N is the refractive index and K is the extinction coefficient related to the absorption coefficient by $K = \alpha\lambda_0/4\pi$. In this case a wave, linearly polarized at $z = 0$, will, after propagating through the medium, be elliptically polarized with the major axis of the ellipse rotated through the angle θ_F. We have $\theta_F = \mathrm{Re}(\Delta/2)$, so

$$\theta_F = (\pi/\lambda_0)\,\mathrm{Re}(n_+ - n_-) = (\pi/\lambda_0)(N_+ - N_-) \qquad (5.4)$$

(2) A difference in absorption coefficient of RCP and LCP light results in an ellipticity η_F, where $\tan\eta_F = \mathrm{Im}(\Delta/2)$. For $\eta_F \ll 1$ one finds

$$\eta_F = (\pi/\lambda_0)(K_+ - K_-) \qquad (5.5)$$

This effect is called Faraday ellipticity or magnetic circular dichroism (MCD).

Often equations (5.4) and (5.5) are combined into an expression for the complex Faraday rotation

$$\theta_F - i\eta_F = (\pi/\lambda_0)(n_+ - n_-) \tag{5.6}$$

If the propagation direction of the light is perpendicular to the magnetization ($\vec{k} \perp \vec{H}$) one has to distinguish between $n_\parallel$ and $n_\perp$, where $n_\parallel$ ($n_\perp$) is the complex refractive index of the light component linearly polarized parallel (perpendicular) to the magnetization. This difference results in two effects.

(3) The Cotton-Mouton effect or Voigt effect or magnetic linear birefringence (MLB):

$$\theta_C = (\pi/\lambda_0)(N_\parallel - N_\perp) \tag{5.7}$$

(4) the magnetic linear dichroism (MLD):

$$\eta_C = (\pi/\lambda_0)(K_\parallel - K_\perp) \tag{5.8}$$

The two last-mentioned effects (MLB and MLD) will be left out of the discussion.

So far we have looked only at the magneto-optic effects in transmitted light. In the case of highly absorbing samples it is often useful to use the reflected radiation. The magneto-optic effects in reflection are known as Kerr effects. We distinguish three different geometries (Fig.5.1). In the polar Kerr effect the magnetization $\vec{M}$ is normal to the reflecting surface. In the longitudinal Kerr effect $\vec{M}$ is parallel to the surface and is in the plane of incidence. In the transverse (or equatorial) Kerr effect $\vec{M}$ is parallel to the surface and is perpendicular to the plane of incidence. For simplicity we will discuss only the polar effect for normal incident light ($\vec{M} \parallel z$). If the amplitude of the incident wave is E_0, and if E_r is the reflected amplitude, the reflection coefficient is given by

$$r = \frac{E_r}{E_0} = -\frac{n-1}{n+1} \tag{5.9}$$

where n is the complex refractive index. For polarized light r can be written as

$$r_\pm = R_\pm e^{i\phi_\pm} \tag{5.10}$$

where $\phi_\pm$ is the phase shift upon reflection. If the incident light is linearly polarized, then the reflected light will be elliptically polarized because the RCP and LCP components will no longer have equal amplitude and the major

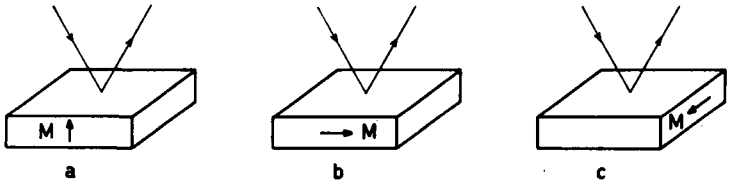

FIG.5.1. Different geometries for measurements of the Kerr effect: (a) polar, (b) longitudinal, (c) equatorial.

axis will be rotated due to the phase difference of the two circular components. This rotation angle is

$$\theta_K = -\frac{1}{2}(\phi_+ - \phi_-) \tag{5.11}$$

The minus sign appears in front of this expression since the reflected light propagates in the negative z direction. The ellipticity is

$$\eta_K = -\frac{R_+ - R_-}{R_+ + R_-} \tag{5.12}$$

We can easily show that in first order the complex Kerr rotation is

$$\theta_K - i\eta_K = i\frac{r_+ - r_-}{r_+ + r_-} \tag{5.13a}$$

so

$$\theta_K = \text{Im} - \left(\frac{r_+ - r_-}{r_+ + r_-}\right)$$

and

$$\eta_K = \text{Re} - \left(\frac{r_+ - r_-}{r_+ + r_-}\right)$$

If we express Eq.(5.13) in terms of n, by using Eq.(5.9) we get

$$\theta_K - j\eta_K = i\frac{n_+ - n_-}{n_+ n_- - 1} \tag{5.13b}$$

5.3. Macroscopic theory

Phenomenologically, magneto-optic effects can be described in terms of the susceptibility (or dielectric) tensor. If we assume an $e^{i\omega t}$ time dependence for $\vec{E}$ and $\vec{H}$, Maxwell's equations can be written as

$$\text{curl}\,\vec{E} = -\vec{\vec{\mu}}\cdot\frac{\delta\vec{H}}{\delta t} = -i\omega\vec{\vec{\mu}}\cdot\vec{H} \tag{5.14a}$$

$$\text{curl}\,\vec{H} = \vec{\vec{\epsilon}}\cdot\frac{\delta\vec{E}}{\delta t} + \vec{J} = i\omega\vec{\vec{\epsilon}}\cdot\vec{E} \tag{5.14b}$$

In principle the current density J may be incorporated in the dielectric tensor, but for the ferrites J = 0, since the conductivity is negligible.

In the microwave region ϵ is a constant ($\epsilon = \epsilon_0$), whereas at optical frequencies $\mu = \mu_0$. We can therefore eliminate $\vec{E}$ from Eqs (5.14) and we obtain: curl curl $\vec{H} = \omega^2\vec{\vec{\epsilon}}\vec{\vec{\mu}}\cdot\vec{H}$, where either $\vec{\vec{\epsilon}}$ or $\vec{\vec{\mu}}$ is constant. We introduce the relative quantity $\vec{\vec{\kappa}} = \vec{\vec{\epsilon}}\,\vec{\vec{\mu}}/\epsilon_0\mu_0 = \vec{\vec{\epsilon}}\,\vec{\vec{\mu}}\,c^2$, so at low frequencies $\vec{\vec{\kappa}}$ is the relative permeability tensor, and at high frequencies $\vec{\vec{\kappa}}$ is the relative dielectric tensor. We get

$$\text{curl curl}\,\vec{H} = -\nabla^2\vec{H} + \nabla(\nabla\cdot\vec{H}) = \frac{\omega^2}{c^2}\vec{\vec{\kappa}}\cdot\vec{H} \tag{5.15}$$

For a plane wave the solutions have the form $\vec{H} = \vec{H}_0\exp(-i\vec{k}\cdot\vec{r})$, where $\vec{k}$ is the propagation vector and $\vec{r}$ the displacement vector. We have $\nabla^2\vec{H} = -k^2\vec{\vec{I}}\cdot\vec{H}$, and $\nabla(\nabla\cdot\vec{H}) = -\vec{k}(\vec{k}\cdot\vec{H})$, where $\vec{\vec{I}}$ is the unit tensor. If we put $\omega/c = k_0 = 2\pi/\lambda_0$, Eq.(5.15) gives

$$k^2\vec{\vec{I}}\cdot\vec{H} - \vec{k}(\vec{k}\cdot\vec{H}) - k_0^2\vec{\vec{\kappa}}\cdot\vec{H} = 0 \tag{5.16}$$

This form of Eq.(5.16) is most convenient when we discuss microwave experiments, where $\vec{H}$ stands for the r.f. magnetic field vector. However, at optical frequencies we normally indicate the wave by means of the $\vec{E}$ vector. In that case $\vec{E}$ simply replaces $\vec{H}$ in Eq.(5.16).

For a further calculation we have to know the $\vec{\vec{\kappa}}$ tensor. For a cubic material with $\vec{M}\parallel z$, this tensor has the form [5.3]

$$\vec{\vec{\kappa}} = \begin{Bmatrix} \kappa_1 & \kappa_2 & 0 \\ -\kappa_2 & \kappa_1 & 0 \\ 0 & 0 & \kappa_3 \end{Bmatrix} \tag{5.17}$$

where the coordinate axes have been taken to lie along the principal axes of the crystal. The off-diagonal elements are linear in $\vec{M}$, the diagonal elements are only dependent on $\vec{M}$ in second order. For the simple case of a wave propagating along the z axis, substitution of (5.17) into (5.16) gives a secular determinant with solutions

$$n_{\pm}^2 = \kappa_1 \pm i\kappa_2 \tag{5.18}$$

Here n denotes the refractive index, $n = k/k_0$. The corresponding solutions for $\vec{H}$ are

$$H_0^x : H_0^y = 1 : \pm i \tag{5.19}$$

The + sign corresponds to an RCP wave, the − sign to an LCP wave. Since the difference between n_+ and n_- is small, we can write

$$n_+^2 - n_-^2 = (n_+ + n_-)(n_+ - n_-) \approx 2n_0(n_+ - n_-)$$

and from Eq.(5.18) we get

$$n_+ - n_- = \frac{i\kappa_2}{n_0} \tag{5.20}$$

where n_0 is the average refractive index. Since $|\kappa_2| \ll |\kappa_1|$, we get from (5.18), $n_0 \approx \kappa_1^{1/2}$. A comparison of (5.6) and (5.20) shows that

$$\theta_F - i\eta_F = (\pi/\lambda_0)\frac{i\kappa_2}{\kappa_1^{1/2}} \tag{5.21}$$

The diagonal element κ_1 is related to the real refractive index N and the extinction coefficient K by means of Eq.(5.3), i.e.

$$N^2 - K^2 = \kappa_1' \text{ and } 2NK = \kappa_1'' \tag{5.22}$$

where κ_1' and κ_1'' are the real and imaginary parts of κ_1. In this way κ_1' and κ_1'' can be expressed in terms of the observables N, K, θ_F and η_F. For the Kerr effect one finds similarly from Eqs (5.20) and (5.13b):

$$\theta_K - i\eta_K = \frac{-\kappa_2}{(\kappa_1 - 1)\kappa_1^{1/2}} \tag{5.23}$$

This means that the transmission effects are a factor of $\pi(\kappa_1 - 1)/\lambda_0$ larger than reflection effects in materials sufficiently transparent to transmit light

through a path of one or more wavelengths. However, in strongly absorbing materials, for which transmission measurements must be made on thin layers, the transmission and reflection effects will be of comparable magnitude.

5.4. Faraday effect in the infrared and microwave regions

In this subsection we consider the contributions to the Faraday effect due to the precessing magnetic moments in the ferrites. Let us first consider a ferromagnetic compound. In a static magnetic field $\vec{H}_0$ the magnetization vector precesses at the frequency

$$\omega_0 = \gamma H_0$$

where γ is the gyromagnetic ratio, $\gamma = g\mu_B/\hbar$.

If a radio-frequency field $\vec{h}$ is applied perpendicular to the d–c field, energy can be transferred from the r–f field to the spin system if the resonance condition is satisfied, i.e. if $\omega = \omega_0$. For $g = 2$, the value of the gyromagnetic ratio becomes $\gamma = 2.8$ MHz/Oersted, i.e. for a static field $H_0 \sim 3000$ Oe the resonance frequency is of the order of 10 GHz.

From the equations of motion we can derive the expressions for the permeability tensor elements that relate the rf magnetization vector $\vec{m}$ to the microwave field $\vec{h}$: $\vec{m} = \vec{\vec{\kappa}} \cdot \vec{H}$. If the static field is taken along the z axis, the tensor has the form of Eq.(5.17). The expressions for the elements of the susceptibility tensor are rather lengthy and we therefore refer to the literature [5.4, 5, 6].

In ferrimagnets we have two (or more) magnetic sublattices which are strongly coupled. It has been shown [5.4] that the resonance condition is entirely analogous to the condition for ferromagnetic resonance if we replace γ by an effective quantity γ_{eff} and the magnetization by the net magnetization of the sublattices:

$$\omega_0 = \gamma_{eff} H_0, \vec{M}_s = \sum_i \vec{M}_i$$

Here $\gamma_{eff} = \Sigma M_i / \Sigma(M_i/\gamma_i)$, where the sum is taken over the sublattices i. At resonance the sublattices precess in the same direction and in phase.

Neglecting damping completely we obtain for the low-frequency region $\omega < \omega_0$:

$$\theta_F = (\pi/\lambda_0)\,\mathrm{Re}(i\kappa_2/\kappa_1^{1/2})$$

$$= \frac{\omega \epsilon^{1/2}}{2c}\left[\left(1 + \frac{\omega_m}{\omega_0 + \omega}\right)^{1/2} - \left(1 + \frac{\omega_m}{\omega_0 - \omega}\right)^{1/2}\right] \qquad (5.24)$$

When $\omega > \omega_0$ the Faraday effect becomes non-dispersive and we obtain under these conditions

$$\theta_F = \frac{\omega_m \epsilon^{1/2}}{2c} = \frac{\epsilon^{1/2}}{2c} \gamma_{eff} 4\pi M_s \tag{5.25}$$

Inserting reasonable values for the constants, $\epsilon \approx 15$, $4\pi M_s \approx 2000$ gauss, we obtain a rotation of approximately 130°/cm. Apart from the ferrimagnetic resonance mode discussed above, another mode of resonance will occur in ferrimagnetics. In this mode, which occurs at much higher frequencies, the sublattices precess in the same rotational direction but out of phase. This resonance is called exchange resonance since it takes place in the exchange field. Because the exchange field is of the order of magnitude of 10^6 Oe, the resonance frequency ω_e is about 3×10^{12} Hz, i.e. a wavelength $\gamma \approx 100$ μm (the far infrared region). For the case of a two-sublattice ferrite, and neglecting the damping terms, the Faraday rotation is described by [5.5]

$$\theta_F = \frac{4\pi\epsilon^{1/2}}{2c} \frac{\omega_e^2 \gamma_{eff} M - \omega^2(\gamma_1 M_1 + \gamma_2 M_2)}{\omega_e^2 - \omega^2} \tag{5.26}$$

as before

$$\gamma_{eff} = \left| \frac{\gamma_1 \gamma_2 \vec{M}}{\gamma_2 \vec{M}_1 + \gamma_1 \vec{M}_2} \right| \qquad \text{and } \vec{M} = \vec{M}_1 + \vec{M}_2$$

Thus, in the frequency region $\omega_0 < \omega \approx \omega_e$, the Faraday rotation is dispersive. Of course, when we are too close to resonance, Eqs (5.24) and (5.26) are inapplicable and damping terms have to be included.

When we proceed to optical frequencies, $\omega \gg \omega_e$, Eq.(5.26) can be simplified to:

$$\theta_F = \frac{2\pi\epsilon^{1/2}}{c} (\gamma_1 M_1 + \gamma_2 M_2) = \frac{2\pi n_0}{c} \sum_i M_i \gamma_i \tag{5.27}$$

Experimentally this equation has been verified for a number of different ferrites. In general good agreement was observed. Measurements at microwave frequencies are more difficult to perform since the experimental values depend strongly on the dimensions of the samples. Nevertheless, extensive use is made of ferrites in microwave devices like rotators and resonance isolators [5.6].

5.5. Magneto-optic effects due to electric dipole transitions

At optical frequencies the main contributions to the magneto-optic effects are due to electric dipole transitions. The components of the dielectric tensor $\vec{\vec{\epsilon}}$ can be derived from the polarizability tensor elements $\vec{\vec{\alpha}}$. From the quantum-mechanical treatment [5.7] it follows that the off-diagonal element has the form

$$i\kappa_2 = \frac{2\pi NL}{\hbar} \sum_{g,n} \rho_g \frac{(\omega - j\Gamma)}{\omega_{ng}^2 - \omega^2 + \Gamma^2 + 2j\omega\Gamma}$$

$$\times \{|p_{ng}^+|^2 - |p_{ng}^-|^2\} \tag{5.28}$$

where g runs over ground states with occupation probability ρ_g, and n runs over excited states at energies $\hbar\omega_{ng}$ above the ground states. N is the number of atoms or ions per unit volume, Γ is half the linewidth at half amplitude of the transition from g to n, and p_{ng} is the matrix element of the electric dipole moment operator $e\vec{r}$ for this transition:

$$p_{ng} = \langle n|e\vec{r}|g\rangle$$

As before, + and − signs are used for RCP and LCP radiation respectively. In a polarizable medium the electric field is modified by the dielectric response of the medium. To account for this local field correction the dielectric constant is multiplied by the Lorentz–Lorenz factor:

$$L = (n^2 + 2)^2/9$$

We first consider the wavelength region in the near infrared, where the spinel and garnet ferrites have a low absorption coefficient. Since we are far from resonance the damping terms can be neglected. From the general expression (5.28) we find the Faraday rotation:

$$\theta_F = K \sum_{n,g} \rho_g \frac{\omega^2}{\omega_{ng}^2 - \omega^2} \{|p_{ng}^+|^2 - |p_{ng}^-|^2\} \tag{5.29}$$

where K is a constant. Crossley et al. [5.8] simplified this expression by considering the states $|g\rangle$ and $|n\rangle$ to be in two closely spaced groups separated by an

energy $\hbar\omega_0$, much greater than the spacing within the groups. If the frequency ω is such that $E_n, E_g \ll \hbar\omega \ll \hbar\omega_0$, where E_n and E_g are the energies of excited and ground states relative to their respective mean energies, the frequency term in (5.29) can be expanded:

$$\frac{\omega^2}{\omega_{ng}^2 - \omega^2} = \frac{\omega^2}{\omega_0^2 - \omega^2}\left(1 - \frac{2\omega_0(E_n - E_g)}{(\omega_0^2 - \omega^2)} + \ldots\ldots\right)$$

since $\hbar\omega_{ng} = \hbar\omega_0 + E_n - E_g$. We recognize three contributions:

$$\theta_F(1) = K_1' \sum_g \rho_g \sum_n \frac{\omega^2}{\omega_0^2 - \omega^2} \{|p_{ng}^+|^2 - |p_{ng}^-|^2\}$$

$$\theta_F(2) = -K_2' \sum_g \rho_g \sum_n \frac{2\omega_0\omega^2 E_n}{(\omega_0^2 - \omega^2)^2} \{|p_{ng}^+|^2 - |p_{ng}^-|^2\} \qquad (5.30)$$

$$\theta_F(3) = K_3' \sum_g \rho_g \sum_n \frac{2\omega_0\omega^2 E_g}{(\omega_0^2 - \omega^2)^2} \{|p_{ng}^+|^2 - |p_{ng}^-|^2\}$$

For paramagnetic ions in an applied field, $\theta_F(1)$ is known as the "paramagnetic" rotation, since it is usually proportional to the magnetic moment of the ion. If the ground state of the ion is orbitally non-degenerate the terms $\theta(1)$ and $\theta(3)$ will vanish. The remaining $\theta_F(2)$ term, which is much smaller than $\theta_F(1)$, is known as the "diamagnetic" rotation.

Crossley et al. investigated the various contributions in Eq.(5.30) for ions in an exchange field. The results of this analysis are: For a ground state with orbital momentum:

$$\theta_F(1) = K_1 \frac{\omega^2}{\omega_0^2 - \omega^2} M \qquad (5.31)$$

where K_1 is a constant and M the magnetic moment of the ion. For a ground state without orbital momentum, i.e. for S states or orbital singlets resulting from the crystal field:

$$\theta_F(1) = -K_2 \frac{\Delta g}{g} \frac{\omega^2}{\omega_0^2 - \omega^2} M$$

$$\theta_F(2) = K_3 \lambda \frac{\omega^2 \omega_0}{(\omega_0^2 - \omega^2)^2} M \qquad (5.32)$$

Δg is the deviation of g from the free spin value $g = 2.002$, λ is the spin-orbit coupling constant for the upper state, and K_2 and K_3 are constants. For true S state ions like Fe^{3+}, Δg will be very small, and we expect only a diamagnetic contribution. However, when the singlet ground state is a result of the crystalline field one often finds that Δg deviates from zero. This can be due to a mixing-in of excited states with a non-zero orbital momentum. In that case there can be an appreciable paramagnetic contribution $\theta_F(1)$ due to the more favourable frequency factor.

At present we can conclude from this analysis that the electric dipole contribution to the Faraday rotation is proportional to the magnetic moment of the ions. It should be recalled here that we reached the same conclusion for the contribution due to the magnetic permeability, Eq.(5.28). This means that in the rare-earth iron garnets (RIG) for instance, the total Faraday rotation can be written as

$$\theta_F = \frac{2\pi n_0}{c} [\gamma_{Fe}(M^t_{Fe} - M^0_{Fe}) - \gamma_R M_R]$$

$$- A(\omega)M^0_{Fe} + B(\omega)M^t_{Fe} - C(\omega)M_R$$

$$= A'M^0_{Fe}(T) + B'M^t_{Fe}(T) + C'M_R(T) \qquad (5.33)$$

In this expression the gyromagnetic ratios for octahedral and tetrahedral iron are put equal. The frequency dependence of A, B and C is given by the frequency dependence of Eqs (31) and (32). In the final form of Eq.(33) we have indicated the temperature dependence of the sublattice magnetization. Since these M(T) values are well known from other measurements, e.g. from NMR or Mössbauer experiments, the temperature dependence of θ_F can be used to determine the constants A', B', C'.

Table 5.I gives values of the electric dipole contributions to the rotation at 1.15 μm as cited in Ref.[5.7]. From this table the ratio $A/B \approx 2$ for YIG and $Gd_3Fe_5O_{12}$ (GdIG), i.e. the octahedral ferric ions contribute about twice as much as the tetrahedral ions in these compounds. However, in $Tb_3Fe_5O_{12}$, where Tb^{3+} has a g factor of 1.5, the Tb contribution is by far the largest. Figure 5.2 shows the results for YIG and GdIG. The rotation of GdIG changes sign at the temperature T_{comp} due to a change in the direction of the magnetization. The cause of this change will be clear from Fig.5.3 which shows the magnetization curves as a function of temperature for the three different magnetic sublattices in GdIG. The gadolinium magnetization is always parallel to the octahedral iron magnetization but due to the different temperature dependence the total magnetization is parallel to the octahedral magnetization

TABLE 5.I. ELECTRIC DIPOLE PARAMETERS AT 1.15 μm

	A	B	C
YIG	-40.3 ± 1.7	-21.4 ± 1.2	
GdIG	-42.4 ± 1.8	-27.1 ± 1.3	-1 ± 0.2
TbIG	-9 ± 15	-10 ± 11	-84.8 ± 2.5

below T_{comp} and antiparallel to it above T_{comp}. Below about 1 μm the absorption coefficient of the ferrites increases rapidly due to crystal field transitions and charge transfer transitions. Therefore, for $\lambda < 1$ μm we have to use Eq.(5.28) including damping. We shall briefly discuss the magneto-optic behaviour in this region.

In a magnetically dilute system there are two cases. If the ground state of the paramagnetic centre has a finite orbital momentum the resulting line shape is called paramagnetic (Fig.5.4). For ions with a non-degenerate ground state but with a finite orbital momentum in an excited state a so-called diamagnetic line shape appears (Fig.5.4). We observe from this figure that the line shapes are entirely different. For the paramagnetic case the Faraday rotation θ_F and Kerr ellipticity η_K have a dispersive shape, whereas the Faraday ellipticity and Kerr rotation show a maximum at the resonant frequency ω_0. The diamagnetic case on the contrary shows dispersive θ_K and η_F and a resonant peak in θ_F and η_K.

In the garnets the crystal field transitions of the Fe^{3+} ions are spin- and electric-dipole-forbidden. The action of the exchange field and spin-orbit coupling makes the transition probabilities $|p^+_{ng}|^2$ and $|p^-_{ng}|^2$ for RCP and LCP radiation different, and the resulting lines have the paramagnetic shape [5.2, 9, 10]. On the other hand, the charge transfer bands in the garnets are due to spin- allowed and dipole-allowed transitions between an orbital singlet and an excited state which is split by the exchange field and spin-orbit coupling. In this case one expects a diamagnetic line shape. This simple model has been used by several investigators to unravel the complicated spectrum of the iron garnets [5.10, 11, 12]. Especially Kahn et al. [5.10] have made an extensive use of this difference in line shape for the interpretation of their experimental data on a large number of iron oxides. Recently, Scott et al. [5.13] have argued that this distinction between allowed and forbidden bands is not allowed. They mention that a paramagnetic line was observed by Cheng, for the allowed charge transfer transition of Fe^{3+} in MgO. A similar observation for Eu^{2+} in CaF_2 was made already by Shen and Bloembergen [5.14]. These observations are supported by the calculations of Crossley et al. [5.8]. On the basis of these results Scott et al. [5.13] argue that previous analyses of

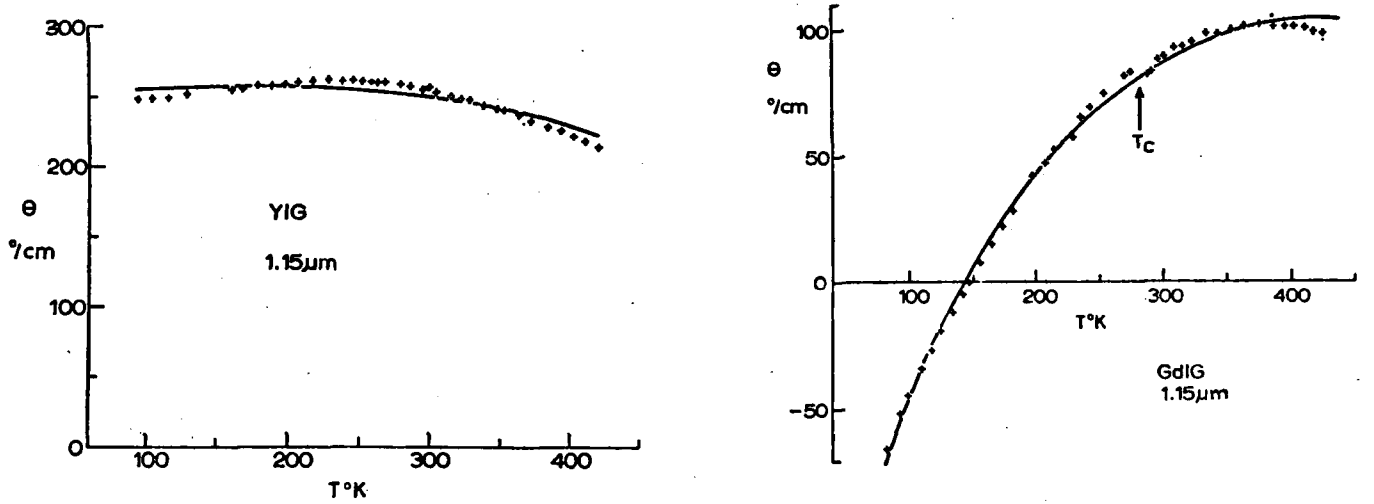

FIG.5.2. Experimental (crosses) and theoretical (solid line) Faraday rotation of YIG and GdIG at 1.15 μm wavelength as a function of temperature. For GdIG the negative of θ is plotted below the compensation temperature T_C (From Ref.[5.8].)

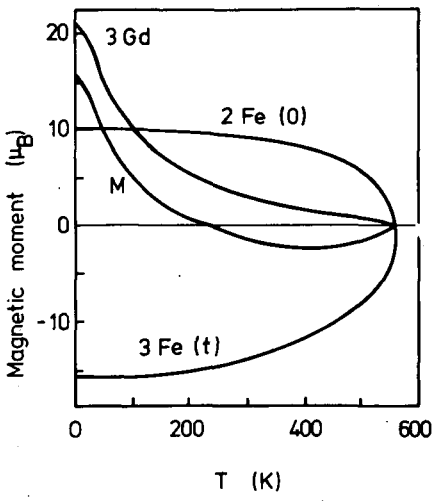

FIG.5.3. Magnetic moment in Bohr magnetons as a function of temperature for the three magnetic sublattices in GdIG. Fe(o) means Fe^{3+} on octahedral sites, Fe(t) Fe^{3+} on tetrahedral sites.

the magneto-optic spectra of iron garnets in the visible and ultraviolet spectral region may be in error.

5.6. Some experimental results

Of the oxides containing Fe^{3+} the rare-earth iron garnets have been investigated most extensively. We will not discuss these experiments in detail, but indicate only a few representative results.

In YIG only the Fe^{3+} transitions contribute to the magneto-optic spectra. Kahn et al. [5.10] have measured the Kerr rotation and ellipticity in the ultraviolet and visible region (1.7 – 5.6 eV). Figure 5.5 shows the results for a single crystal of YIG at room temperature. From reflectivity measurements the diagonal elements κ_1 and the complex refractive index n were calculated (Fig.5.6). From the combined data of Figs 5.5 and 5.6 the off-diagonal elements κ_2 were obtained (Fig.5.7). The transitions in the region 1.2–3.0 eV have been discussed by Scott et al. [5.13]. Absorption spectra, magnetic circular dichroism and Faraday rotation data at 77K are used to investigate the nature of the ferric transitions in this region.

The influence of the sublattice magnetization is evident from the Kerr rotation data [5.10] shown in Fig.5.8. In $Eu_3Fe_5O_{12}$ the tetrahedral iron ions

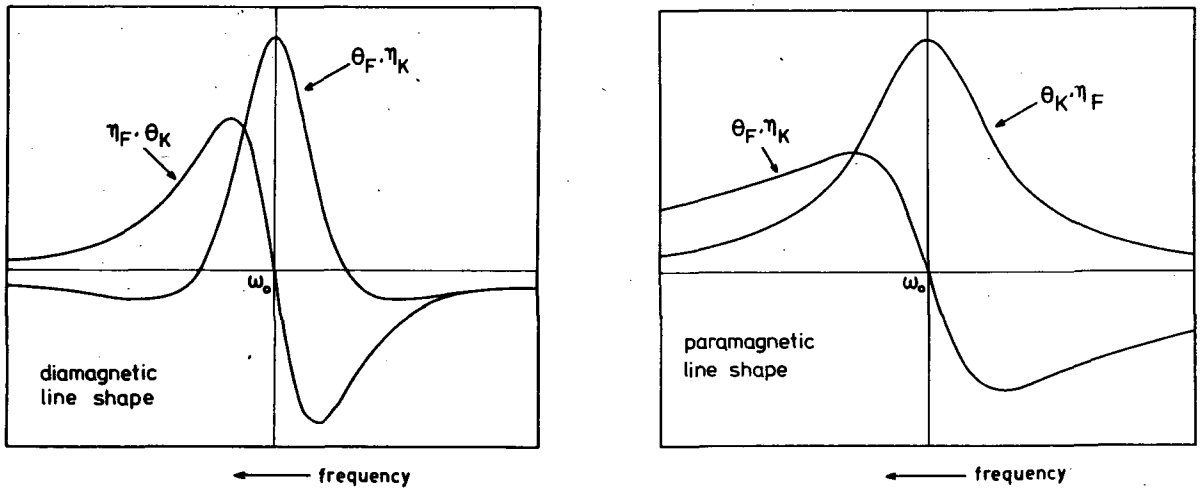

FIG.5.4. Line shapes for Faraday rotation θ_F, Faraday ellipticity η_F, Kerr rotation θ_K and Kerr ellipticity η_K.

Left: diamagnetic line shape,
right: paramagnetic line shape.

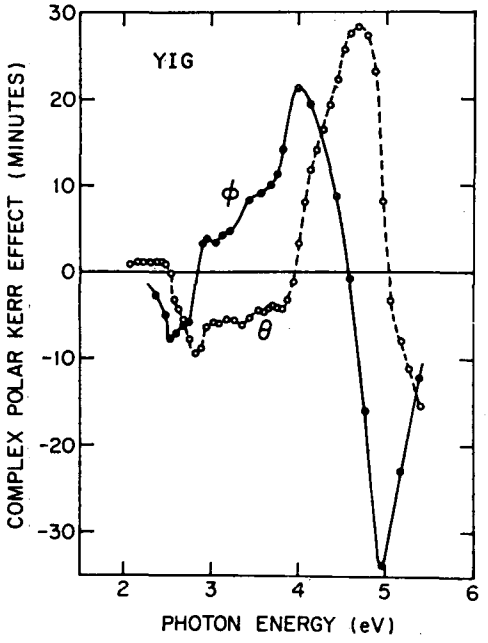

FIG.5.5. Complex polar Kerr effect, rotation ϕ, ellipticity θ, for YIG (110) face. (From Ref.[5.10].)

are partly replaced by diamagnetic Ga^{3+} ions. If the gallium ions are on tetrahedral sites exclusively, the octahedral and tetrahedral sublattice magnetizations are equal when $x = 1$ in $Eu_3Fe_{5-x}Ga_xO_{12}$. For $x > 1$ the total magnetization is in the same direction as the octahedral magnetization. Near the compensation point the Kerr rotation reverses its sign. The Faraday rotation in the visible and near infrared is very important for practical applications. For a modulator the relevant device parameter is the Faraday rotation per dB intensity loss. Several investigators, therefore, have tried to improve this so-called "figure of merit" by suitable substitutions in YIG. Below the absorption edge ($\hbar\omega < 2.5$ eV) pure YIG has a small positive Faraday rotation which is due mainly to the tail of an absorption band near 4.1 eV. Partial replacement of Y^{3+} by Bi^{3+} leads to a considerable increase in oscillator strength of transitions near 2.8 eV and 3.3 eV. [5.11]. It is assumed that the large spin-orbit coupling of the Bi^{3+} is responsible for this increase. As a result the Faraday rotation in the visible and near infrared is increased considerably and is of opposite sign (Fig.5.9).

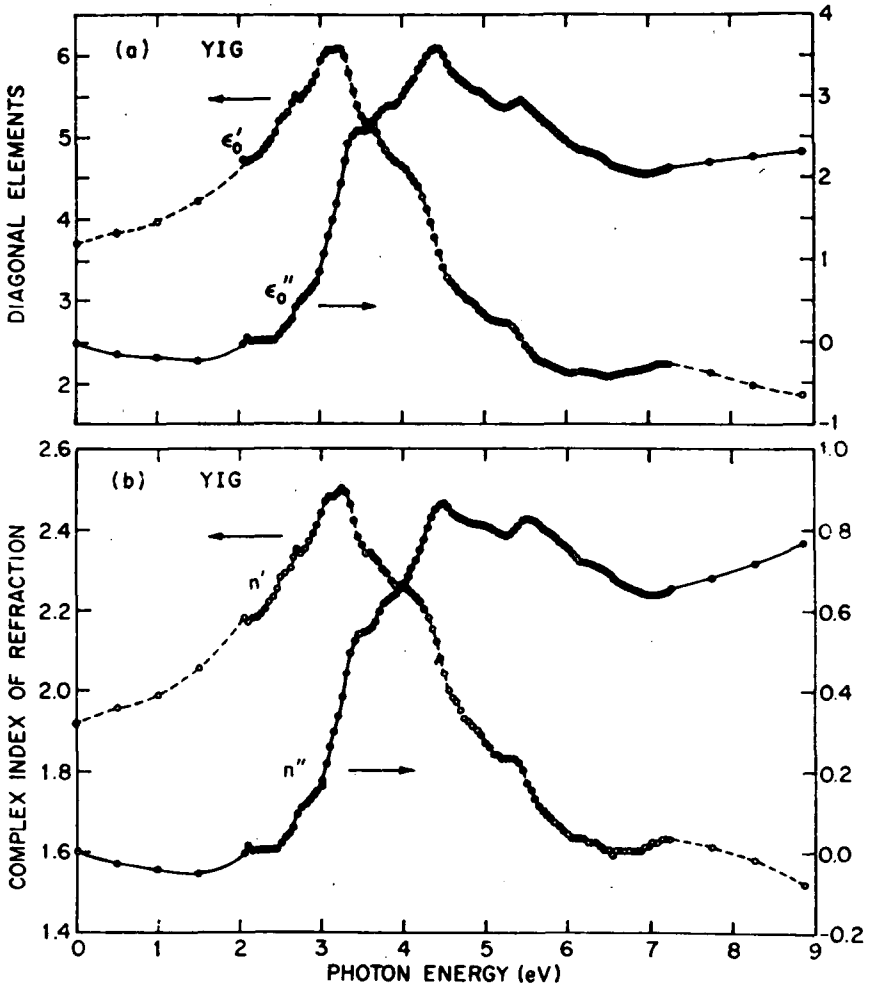

FIG.5.6. Complex diagonal elements $\epsilon_0 = \epsilon_0' + i\epsilon_0''$ (in the text $\kappa_1 = \epsilon_0$), and complex refractive index $n = n' + in''$ (in our text $n' = N$, $n'' = K$), for YIG. (From Ref.[5.8].)

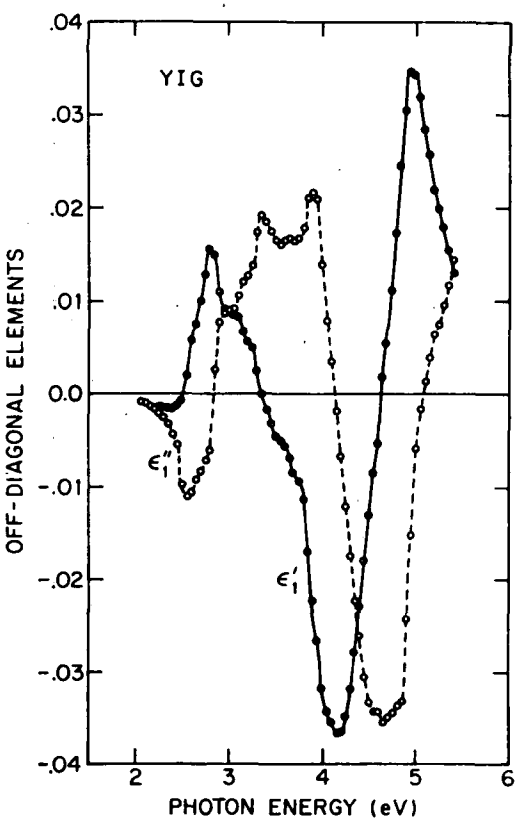

FIG.5.7. Off-diagonal elements $\epsilon_1 = \epsilon_1' + i\epsilon_1''$ for YIG. In the text $\epsilon_1 = i\kappa_2$. (From Ref.[5.10].)

Finally, a comment on the magneto-optic effects in spinel ferrites. In the spinel $NiFe_2O_4$ the major rotation peaks are found at 4 and 5 eV [5.10]. These energies coincide with the principal rotation peaks for the garnets (cf. Fig.5.5). By analogy with the assignment of the garnet peaks, Kahn et al. associated the 4 eV and 5 eV rotations in the spinel with transitions in the Fe^{3+}_{oct} and Fe^{3+}_{tetr} sublattices, respectively. The signs of the rotations in $NiFe_2O_4$ are opposite to the signs of the rotations in the garnets, as would be expected from the reversed alignments of the corresponding garnet and spinel Fe^{3+} sublattices in an external magnetic field. An extra rotational peak at 1.06 eV is attributed to a transition of the Ni^{2+} ions [5.15]. A large Faraday rotation associated with a tetrahedral Co^{2+} crystal field transition has recently been reported in substituted cobalt ferrites [5.16].

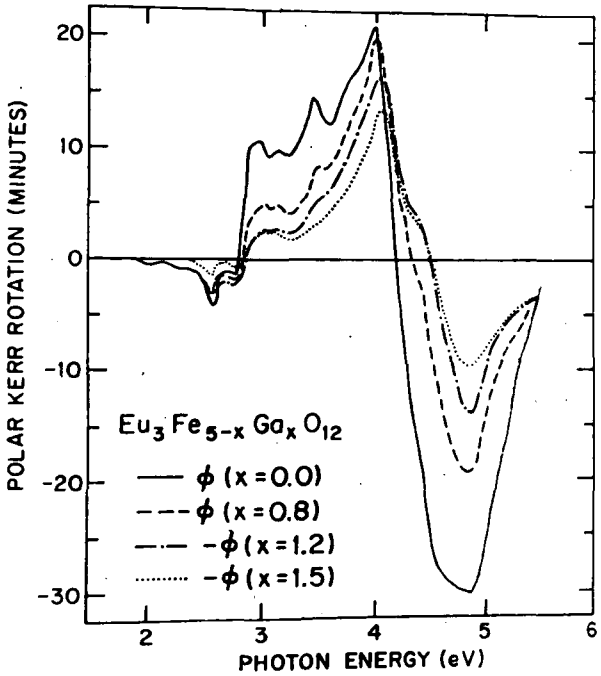

FIG.5.8. Polar Kerr rotation for $Eu_3Fe_{5-x}Ga_xO_{12}$ ($0 \leqslant x \leqslant 1.5$). The Kerr rotation changes its sign for x between 0.8 and 1.2. (From Ref. [5.10]).

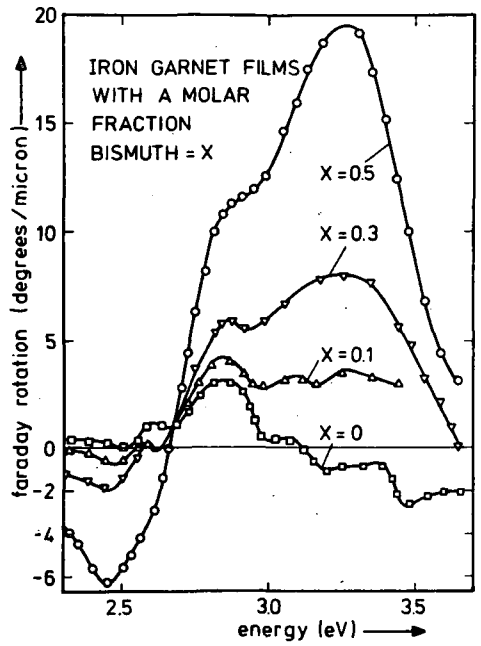

FIG.5.9. Faraday rotation of thin films of Bi-substituted iron garnet, $Y_{3-x}Bi_xFe_5O_{12}$. (From Ref.[5.11].)

REFERENCES TO SECTION 5

[5.1] FREISER, M.J., IEEE Trans. Magn., Mag. **4** (1968) 152.
[5.2] SUITS, J.C., IEEE Trans. Magn., Mag. 8 (1972) 95.
[5.3] LANDAU, L.D., LIFSCHITZ, E.M., Electrodynamics of Continuous Media, Pergamon Press, London (1960).
[5.4] WANGSNESS, R.K., Phys. Rev. **95** (1954) 339.
[5.5] FRAYNE, P.G., Brit. J. Appl. Phys. (J. Phys. D.) **1** (1968) 741.
[5.6] LAX, B., BUTTON, K.J., Microwave Ferrites and Ferrimagnetics, McGraw-Hill, New York (1962).
[5.7] SHEN, Y.R., Phys. Rev. **133** (1964) A511.
[5.8] CROSSLEY, W.A., COOPER, R.W., PAGE, J.L., STAPELE, R.P., Phys. Rev. **181** (1969) 896.
[5.9] CLOGSTON, A.M., J. Phys. Radium **20** (1959) 151.
[5.10] KAHN, F.J., PERSHAN, P.S., REMEIKA, J.P., Phys. Rev. **186** (1969) 891.
[5.11] WITTEKOEK, S., POPMA, T.J.A., ROBERTSON, J.M., BONGERS, P.F., Phys. Rev. **B12** (1975) 2777.
[5.12] WETTLING, W., ANDLAUER, B., KOIDL, P., SCHNEIDER, J., TOLKSDORF, W., Phys. Status Solidi **B59** (1973) 63.
[5.13] SCOTT, G.B., LACKLISON, D.E., RALPH, H.I., PAGE, J.L., Phys. Rev. **B12** (1975) 2562.
[5.14] SHEN, Y.R., BLOEMBERGEN, N., Phys. Rev. **133** (1964) A515.
[5.15] ZANMARCHI, G., BONGERS, P.F., J. Appl. Phys. **40** (1969) 1230.
[5.16] AHRENKIEL, R.K., COBURN, T.J., PEARLMAN, D., CARNALL, E., Jr., MARTIN, T.W., LYU, S.L., AIP Conf. Proc. **24** (1975) 186.